Lascala
Erasmus Mundus Master

Transient Diffuse Scattering in GeSbTe as a Timing Tool for Ultrafast X-ray Diffraction

Masters Thesis

Sally Dolan

Supervised by Jörgen Larsson

Spring Semester 2026

LUND UNIVERSITY

LTH
FACULTY OF ENGINEERING

université PARIS-SACLAY

Erasmus+

SZTE
UNIVERSITY OF SZEGED

Abstract

Precise determination of the time of simultaneous incidence of laser pump and X-ray probe pulses is essential for ultrafast X-ray diffraction experiments. This work investigates the use of diffuse scattering from the phase-change material $Ge_2Sb_2Te_5$ (GST) as a timing tool for pump-probe measurements at the FemtoMAX beamline at MAX IV Laboratory.

A complete data analysis pipeline was developed to process time-resolved powder diffraction data. Individual detector images were sorted into pump-probe delay bins using the jitter monitors at FemtoMAX, azimuthally integrated using the `pyFAI` software package, and combined to produce time-resolved scattering profiles.

Measurements obtained during three experimental campaigns reproduced the characteristic ultrafast increase in diffuse scattering intensity following femtosecond laser excitation of GST. By combining data from multiple delay scans, the intensity increase was resolved to occur within 70 fs, consistent with previous measurements at FemtoMAX. The impact of laser fluence and sample temperature on the diffuse scattering response was also investigated, with the signal becoming difficult to resolve at low excitation fluences.

These results demonstrate that transient diffuse scattering from GST provides a reproducible marker of time zero for ultrafast X-ray diffraction experiments in a variety of experimental conditions. The analysis framework developed in this work provides a reliable methodology for processing future pump-probe diffraction measurements, and supports the continued use of GST as a time-zero monitor at FemtoMAX.

LRAP number: LRAP632(2026)

Acknowledgements

I would like to thank my supervisor Jörgen Larsson for the opportunity to work on this project, and for your guidance and teaching throughout. Thank you Isa and Eric for always being around to answer my questions, and help with whatever I needed.

The staff at FemtoMAX, Andrius Jurgilaitis, David Kroon, Carl Ekström and Byungnam Ahn each took time to teach me about the facility, and introduce me to their analysis tools. I appreciate their kindness and patience during my time there.

Thank you Malin for working alongside me- your company and support have been so valuable to me. Thank you Yash for always making time to stop by our office. Your many (many) questions helped me to wrap my head around the material, and your curiosity and enthusiasm are infectious.

My friends at home, in my Masters programme, and in Lund have supported me no matter where I've been. I could not have completed this work without them. My parents have encouraged me in every way to pursue my education, and my brother Eoin and his partner Dani have been constant inspirations to me.

Go raibh míle maith agaibh.

Popular Science Summary

Ultrafast X-ray diffraction is a powerful technique for observing how materials change on extremely short timescales. By using a short laser pulse to excite a material and an X-ray pulse to measure it, scientists can measure structural changes occurring within trillionths of a second. To interpret these measurements, it is important to know exactly when the laser and X-ray pulses hit the sample simultaneously. This moment is known as time zero.

This thesis investigates whether the material germanium-antimony-tellurium (GST) can be used as a reliable time-zero monitor at the FemtoMAX beamline at MAX IV Laboratory in Lund. GST is a phase-change material that exhibits a rapid change in its X-ray scattering after being excited by a laser pulse. This fast signal can then be used to pinpoint time zero.

A data-analysis pipeline was developed to process thousands of individual X-ray detector images and sort them according to the timing delay between the pulses. The images were then analysed to track changes in the X-ray signal following laser excitation. Measurements from several experimental campaigns reproduced a rapid increase in scattering, as was previously observed in GST. The response was investigated under different laser fluences, sample compositions, temperatures and X-ray incidence angles.

The results show that GST produces a reproducible, and sufficiently fast response to be used as a time-zero monitor for ultrafast X-ray diffraction experiments at FemtoMAX.

Contents

List of Figures

List of Tables

Introduction

Time-resolved X-ray diffraction is an important technique for investigating photo-induced structural dynamics in condensed matter systems. Using femtosecond pulses, these dynamics can be observed on the time-scale of atomic motions [1]. Applications include mapping photo-induced atomic motion [2, 3], phase transitions [4–6], coherent phonons [7–9], and coupling between these behaviours [10, 11].

As most X-ray detectors are not capable of resolving sub-picosecond timescales, most time-resolved X-ray diffraction experiments utilise a pump-probe scheme. A pump pulse causes a perturbation in the sample, to probe the sample, an X-ray pulse which is short compared to the timescale of the induced structural dynamics is required. The scattered intensity provides a snapshot of the instantaneous structure of the material. By measuring the scattering from the X-ray pulse at many time delays, the time evolution of the sample structure after the perturbation can be reconstructed [1, 12].

In such experiments, resolving a time-zero, the time when the pump and probe beams are simultaneously incident on the sample, is of vital importance. The time zero is used as a reference for all measured pump-probe delays. Without this value, it can be unclear which experimental observations are indeed a result of laser-induced dynamics.

In the early 2000s, sources for femtosecond X-ray pulses began to emerge. Electron beam slicing involves using a femtosecond laser to transversely modulate a thin slice of electrons in a synchrotron storage ring. These electrons are then separated, and used in a bending magnet or undulator to create fs X-ray pulses [13, 14]. Another method from this time involves creating a plasma with a fs laser, which then emits incoherent fs X-ray pulses [15]. For experiments using these methods, the pump and probe pulses are inherently synchronised, but probe flux is low.

Modern X-ray free electron lasers (XFELs) can be optimised for short-pulse generation, providing femtosecond X-ray pulses with much higher flux per pulse [12]. These include the Linac Coherent Light Source (LCLS) in the United States [16], SACLA in Japan [17], Pohang Accelerator Laboratory XFEL in the Republic of Korea [18], European XFEL in Germany [19], and SwissFEL in Switzerland [20].

At XFEL sources, the X-ray pulse is sufficiently brilliant to induce a rapid change of the optical reflectivity or transmittance of a semiconductor material, which is

probed by the laser pulse. This was pioneered at the FEL in Hamburg (FLASH) using XUV/soft X-rays [21, 22]. This technique was further developed at LCLS, SLAC [23–25], and European XFEL [26, 27].

The MAX IV synchrotron in Lund, Sweden features two electron storage rings operated at 3 GeV and 1.5 GeV and optimised for the hard X-ray and soft X-ray/VUV spectral ranges, respectively. A 3 GeV linear accelerator (LINAC) injects both rings, as well as the short pulse facility, with accelerated electron bunches [28].

The only beamline at the short pulse facility is FemtoMAX. Electron pulses from the LINAC pass two 5 m long, tunable undulators generating ultrashort (<100 fs) X-ray pulses with a maximum 7×10^6 photons per pulse at 8 keV. An ultrafast laser system is located in a laser laboratory directly above the beamline. The laser oscillator is phase-locked to the 3 GHz radiofrequency (RF) signal originating from the master oscillator [29].

At FemtoMAX, the X-ray flux is insufficient to pump a sample, inducing measurable changes in optical properties. An alternative is to use standardised reference materials with known temporal responses at the sample position. The faster the dynamics of the sample, the more accurately time zero can be determined. These samples include Bismuth [30, 31], and InSb [32]. These are single crystals, which must be carefully aligned to produce the desired Bragg reflection.

When FemtoMAX was used to analyse a powder sample of the phase-change material $Ge_2Sb_2Te_5$ (GST), an increase in diffuse scattering between two of its diffraction peaks was seen to occur within 70 fs [33]. The study of GST as a timing monitor is therefore of significant interest to further study of ultrafast dynamics at FemtoMAX. The purpose of this work is to verify the presence of the transient diffuse scattering, and to determine its potential as a time-zero monitor in X-ray pump-probe experiments.

Thesis Overview

This thesis work is built around a set of experiments using powder diffraction to determine the utility of $Ge_2Sb_2Te_5$ (GST) as a time-zero monitor at FemtoMAX. In chapter 1, I review the basic theory of X-ray scattering of matter, leading to a description of powder diffraction.

In chapter 2, I provide an overview of the FemtoMAX beamline at MAX IV, where these experiments took place. I discuss the experimental methods used to investigate the GST samples. I describe the timing diagnostics used to determine the relative arrival time of the pump and probe pulses. I introduce the GST samples, and experimental conditions used during our three measurement campaigns.

In chapter 3, I discuss my Python analysis pipeline built to transform our raw data to intensity traces as a function of time over the region of interest.

In chapter 4, I present our experimental results from each of the three experimental campaigns following this analysis. I investigate the dependence of the fast increase in diffuse scattering signal following laser excitation on laser fluence, sample composition, and temperature.

In chapter 5, I discuss our results, and assess the suitability of GST as a time-zero monitor for ultrafast X-ray pump-probe experiments at FemtoMAX.

Chapter 1

Theory

1.1 X-ray Scattering

When an atom is probed by an X-ray beam, its electrons can either absorb the beam, or undergo scattering. Scattered radiation can be studied to determine the properties of the target atom. This comprises both elastic (scattered radiation at same wavelength as incident field), and Compton scattering (scattering at longer wavelength). Since it is elastic scattering that gives rise to Bragg reflections, only this process is of detailed in this work. This discussion follows "X-ray Diffraction" by B.E. Warren [1].

1.1.1 Single Free Electron Scattering

Firstly, taking an unpolarised X-ray beam falling on a single free electron. The electric field in some direction E_0 can be decomposed into polarisation components E_x and E_y. The instantaneous values of the electric field at the interaction point are then

$$\begin{aligned} \epsilon_{0x} &= E_{0x}\sin(\omega t) \\ \epsilon_{0y} &= E_{0y}\sin(\omega t) \end{aligned} \tag{1.1}$$

where ω is the angular frequency of the probe beam. The electric field then exerts a force, inducing an acceleration, a, in the xy plane, once again taking the orthogonal components separately

$$\begin{aligned} a_x &= \frac{f_x}{m_e} = \frac{eE_{0x}\sin(\omega t)}{m_e} \\ a_y &= \frac{f_y}{m_e} = \frac{eE_{0y}\sin(\omega t)}{m_e} \end{aligned} \tag{1.2}$$

where e and m are the electron charge and mass respectively. The electric field induced by an accelerating electron is

$$\epsilon = \frac{e}{4\pi\epsilon_0 c^2|\mathbf{r}|}a\sin(\alpha) \tag{1.3}$$

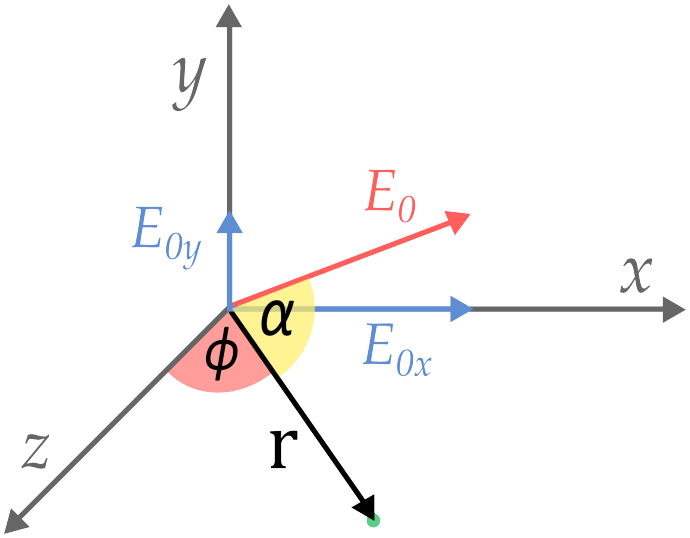

Figure 1.1: Scattering by a single electron at the origin due to incident field E_0

for an observer at $\mathbf{r}$. The component of acceleration perpendicular to $\mathbf{r}$ is $a\sin(\alpha)$. The electric field for an observer in the xz plane at azimuthal angle ϕ

$$\begin{aligned} E_{x'} &= \frac{1}{4\pi\epsilon_0}\frac{e^2}{m_e c^2|\mathbf{r}|}E_{0x}\cos\phi \\ E_{y'} &= \frac{1}{4\pi\epsilon_0}\frac{e^2}{m_e c^2|\mathbf{r}|}E_{0y} \end{aligned} \tag{1.4}$$

and the electric field amplitude at the point of observation

$$E^2 = E_{x'}^2 + E_{y'}^2 = \frac{1}{16\pi^2\epsilon_0^2}\frac{e^4}{m_e^2 c^4|\mathbf{r}|^2}(E_{0x}^2\cos^2\phi + E_{0y}^2) \tag{1.5}$$

In the case of an unpolarised beam, E_0 will take all values in xy with equal probability

$$\begin{aligned} \langle E_0^2\rangle &= \langle E_{0x}^2\rangle + \langle E_{0y}^2\rangle \\ \frac{1}{2}\langle E_0^2\rangle &= \langle E_{0x}^2\rangle = \langle E_{0y}^2\rangle \end{aligned} \tag{1.6}$$

then using equation 1.5;

$$\begin{aligned} \langle E^2\rangle &= \frac{1}{16\pi^2\epsilon_0^2}\frac{e^4}{m_e^2 c^4|\mathbf{r}|^2}[\frac{1}{2}\langle E_0^2\rangle\cos^2\phi + \frac{1}{2}\langle E_0^2\rangle] \\ &= \frac{1}{16\pi^2\epsilon_0^2}\frac{e^4}{m_e^2 c^4|\mathbf{r}|^2}\langle E_0^2\rangle(\frac{1+\cos^2\phi}{2}) \end{aligned} \tag{1.7}$$

The observable quantity here is the optical intensity, which can be substituted into equation 1.7 to obtain the observed scattering intensity as follows,

$$I = \frac{c\epsilon_0}{2}\langle E^2\rangle \tag{1.8}$$

$$I = I_0 \frac{1}{16\pi^2\epsilon_0^2} \frac{e^4}{m_e^2 c^4 |\mathbf{r}|^2} [\frac{1+\cos^2\phi}{2}] \tag{1.9}$$

The factor $(1+\cos^2\phi)/2$ is the polarisation factor for an unpolarised probe beam. For the results presented in this work, a horizontally polarised X-ray beam was used. Since $E_{0y} = 0$, the polarisation factor becomes $\cos^2\phi$ and the intensity of the scattered radiation

$$I = I_0 \frac{1}{16\pi^2\epsilon_0^2} \frac{e^4}{m_e^2 c^4 |\mathbf{r}|^2} \cos^2\phi \tag{1.10}$$

1.1.2 Scattering by an Atom

Scattering from a group of n electrons confined in a small volume, as in an atom, can now be considered. Each electron has some position $\mathbf{r}_n$ close to atomic origin O. The wave-front of an x polarised beam with amplitude E_0 in the direction of unit vector $\mathbf{s}_0$ is incident through O. The scattering intensity measurable at P, some distance $R >> |\mathbf{r}_n|$ in the direction of unit vector $\mathbf{s}$ can be calculated. The instantaneous field at $\mathbf{r}_n$ has travelled an additional d_1 and therefore collects a phase term

$$\epsilon_0 = E_0 \cos(\omega t - k d_1) \tag{1.11}$$

where the wave-number $k = 2\pi\omega/c$. The instantaneous electric field at P due to electron n is

$$\epsilon_n = \frac{E_0 e^2}{4\pi\epsilon_0 m_e c^2 d_2} \cos(\omega t - k(d_1 + d_2)) \tag{1.12}$$

The path length $d_1 + d_2$ can be simplified since the electrons distance from O is

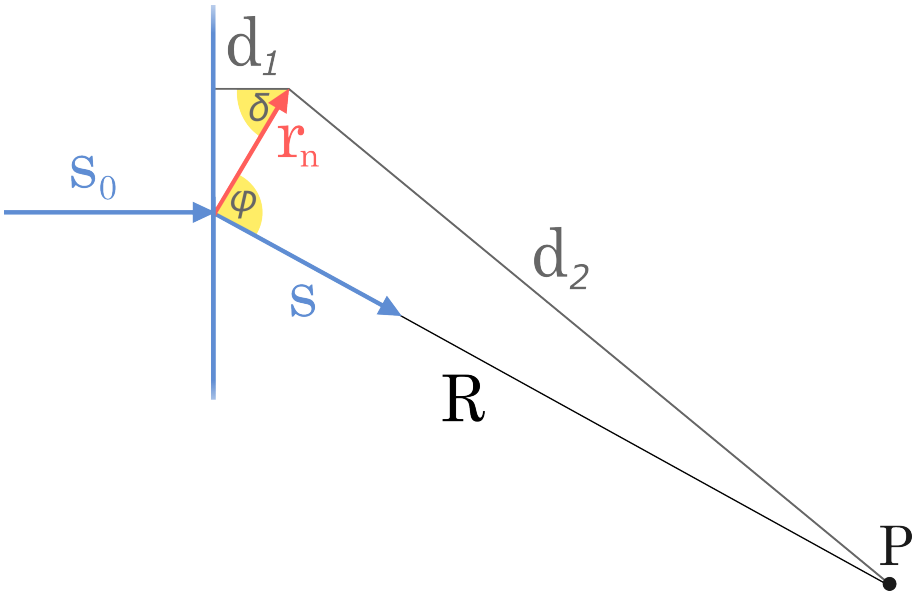

Figure 1.2: Scattering by a wavefront in the direction of unit vector s_0 incident on a group of electrons at $\mathbf{r}_n$ measured at observation point P.

much less than the observation distance R. Since d_1 is the length of the projection

of $|\mathbf{r}_n|$ onto $\mathbf{s}_0$, it can be stated as a dot product

$$\begin{aligned} d_1 = \mathbf{r}_n \cdot \mathbf{s}_0 &= |\mathbf{r}_n| \cos\delta \\ \mathbf{r}_n \cdot \mathbf{s} &= |\mathbf{r}_n| \cos\varphi \end{aligned}$$

Using the law of cosines, and that $|\mathbf{r}_n|^2 << R$,

$$\begin{aligned} d_2^2 = |\mathbf{r}_n|^2 + R^2 - 2|\mathbf{r}_n| R\cos\varphi &\approx R^2 - 2R\mathbf{r}_n \cdot \mathbf{s} \\ d_2 \approx \sqrt{R^2 - 2R\mathbf{r}_n \cdot \mathbf{s}} &\approx R - 2R\mathbf{r}_n \cdot \mathbf{s} \\ d_1 + d_2 \approx R - \mathbf{r}_n \cdot \mathbf{s} + \mathbf{r}_n \cdot \mathbf{s}_0 &= R - (\mathbf{s} - \mathbf{s}_0) \cdot \mathbf{r}_n \end{aligned}$$

Substituting this into equation 1.12,

$$\epsilon_n = \frac{E_0 e^2}{4\pi\epsilon_0 m_e c^2 d_2} \cos(\omega t - k(R - (\mathbf{s} - \mathbf{s}_0) \cdot \mathbf{r}_n)) \tag{1.13}$$

Using the complex representation,

$$\epsilon_n = \frac{E_0 e^2}{4\pi\epsilon_0 m_e c^2 d_2} e^{i\omega t - ik(R - (\mathbf{s}-\mathbf{s}_0)\cdot\mathbf{r}_n)} \tag{1.14}$$

The total field at P is the sum of contributions from each electron,

$$\epsilon = \frac{E_0 e^2}{4\pi\epsilon_0 c^2 d_2} e^{i(\omega t - kR)} \sum_n e^{ik(\mathbf{s}-\mathbf{s}_0)\cdot\mathbf{r}_n} \tag{1.15}$$

Each electron can be treated as a diffuse cloud of charge density ρ in volume dV such that the $\int \rho \, dV = 1$ for each electron, the above sum can be replaced with an integral over charge elements $\rho \, dV$ at $\mathbf{r}$

$$\epsilon_e = \frac{E_0 e^2}{4\pi\epsilon_0 m_e c^2 d_2} e^{i(\omega t - kR)} \int e^{ik(\mathbf{s}-\mathbf{s}_0)\cdot\mathbf{r}} \rho dV \tag{1.16}$$

Where the amplitude of classical scattering per electron

$$f_e = \int e^{ik(\mathbf{s}-\mathbf{s}_0)\cdot\mathbf{r}} \rho dV = \int e^{i(\mathbf{k}-\mathbf{k}_0)\cdot\mathbf{r}} \rho dV \tag{1.17}$$

Thus, the scattering amplitude is given by the Fourier transform of the electron density, evaluated at the scattering vector $\mathbf{q} = \mathbf{k} - \mathbf{k}_0$. Since the observed intensity is proportional to the squared magnitude of the scattered field,

$$I_e \propto |\epsilon_e|^2 = \left(\frac{E_0 e^2}{4\pi\epsilon_0 m_e c^2 d_2}\right)^2 |f_e|^2 . \tag{1.18}$$

1.2 Crystallography

This discussion follows "Introduction to Solid State Physics" by Kittel [2]. A crystal is a repeating structure of some unit cell of atoms, identical under translation along ($\mathbf{a}_1$, $\mathbf{a}_2$, $\mathbf{a}_3$). These vectors define an array of discrete points known as the Bravais lattice. Here, unit cells are labelled by 3 integers m_1, m_2, and m_3 such that the position of an atom n in the crystal is given by

$$R_m^n = m_1\mathbf{a}_1 + m_2\mathbf{a}_2 + m_3\mathbf{a}_3 + \mathbf{r}_n \tag{1.19}$$

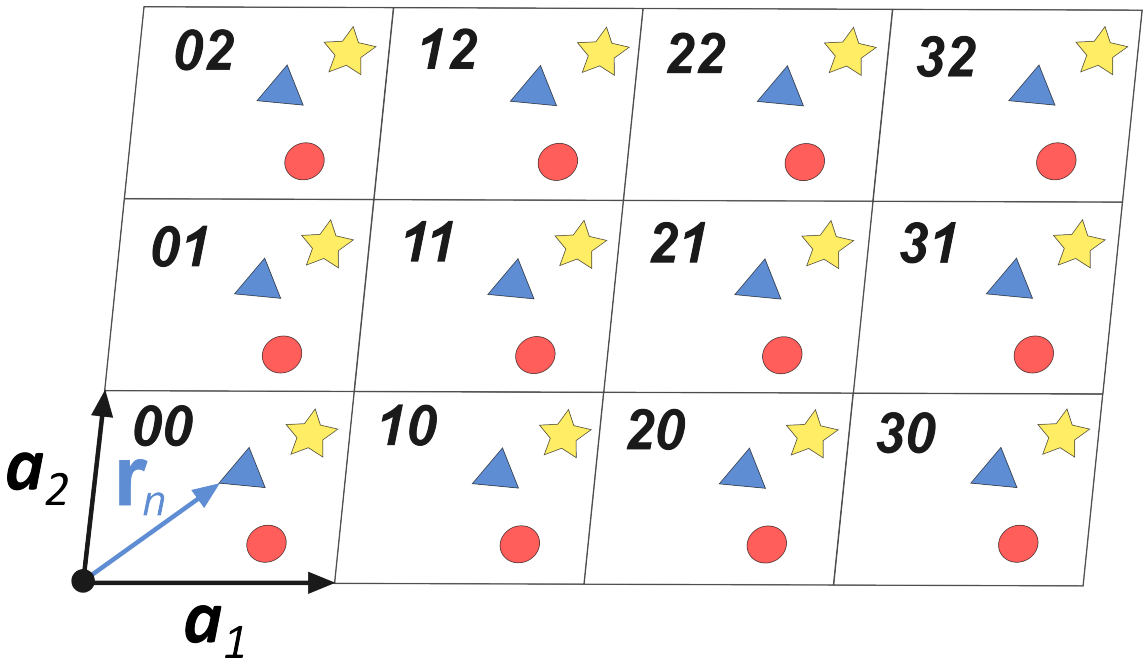

Figure 1.3: 2D crystal with unit cells labelled m_1m_2 characterised by lattice vectors $\mathbf{a}_1$ and $\mathbf{a}_2$. The position of atom n, represented by the blue triangle, is given by the vector $\mathbf{r}_n$.

A primitive unit cell is the smallest cell that, when the translation vectors are applied, reproduces the full lattice. Conventional unit cells are often chosen for convenience, with volume an integer multiple of the primitive unit cell volume.

Crystallographic planes are sets of parallel, equidistant planes, each passing through the origin with the next plane in the set intercepting with the crystallographic axes at $\mathbf{a}_1/h$, $\mathbf{a}_2/k$, $\mathbf{a}_3/l$. The Miller indices hkl of crystallographic planes in a cubic unit cell are shown in figure 1.4.

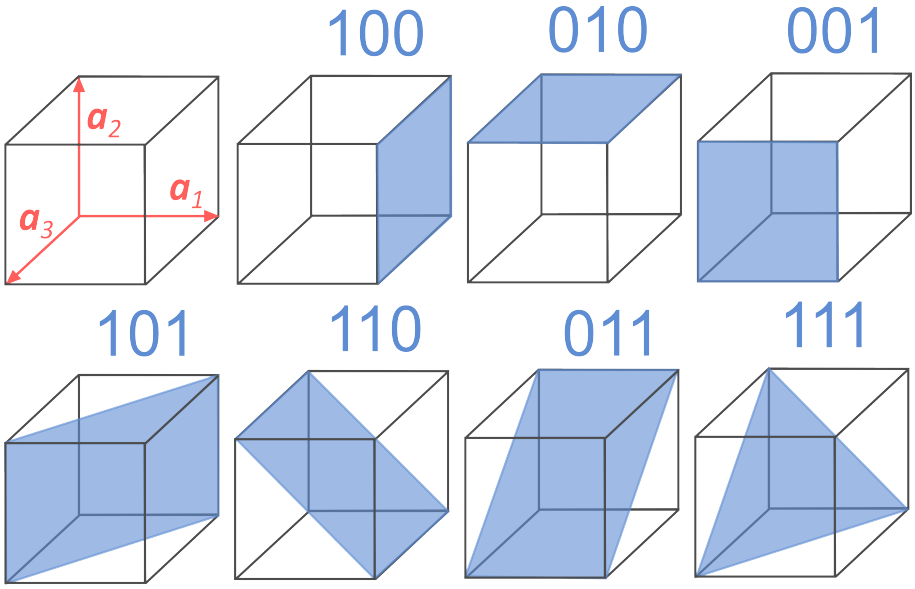

Figure 1.4: Crystallographic planes in a cubic unit cell labelled by their Miller indices hkl defined by intercepts with the lattice vectors $\mathbf{a}_1$, $\mathbf{a}_2$, $\mathbf{a}_3$.

For diffraction from a crystal to be measured, the waves reflected by successive crystallographic planes must interfere constructively. This means that the path difference shown in figure 1.5 must be some integer multiple m of the incident wavelength λ,

$$2\mathrm{d}_{hkl}\sin\theta = m\lambda \tag{1.20}$$

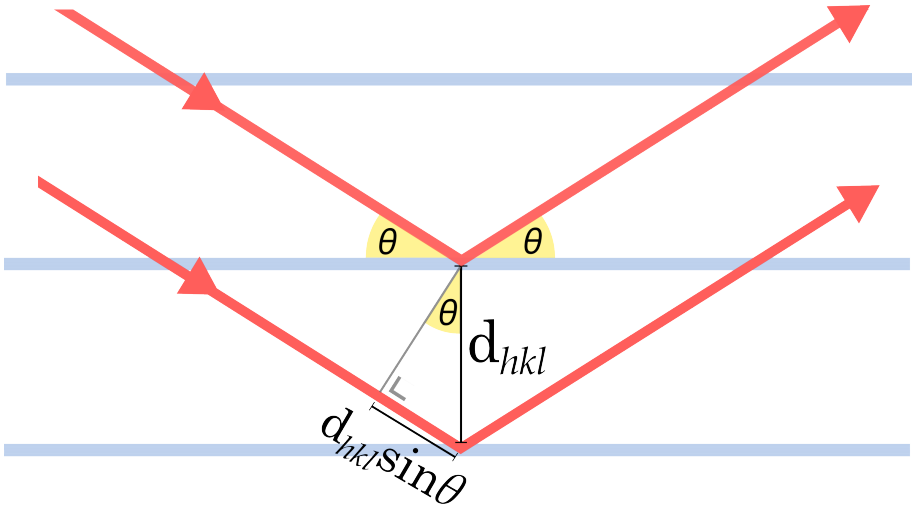

Figure 1.5: The path of an incoming beam at angle θ is shown to have path length difference $2d_{hkl}\sin\theta$ between reflections from two successive planes separated by a distance d_{hkl}.

This is Bragg's law, which can be used to predict when constructive interference will give rise to intensity peaks in the observation plane corresponding to some Bragg

angle θ for each family of crystallographic planes hkl. The intensity peaks arise directly from the periodicity of the crystal structure, and not from the properties of the atoms and molecules inside each unit cell.

The reciprocal lattice vectors $\mathbf{b}_1\mathbf{b}_2\mathbf{b}_3$ are defined as

$$\mathbf{b}_1 = 2\pi\frac{\mathbf{a}_2 \times \mathbf{a}_3}{\mathbf{a}_1 \cdot \mathbf{a}_2 \times \mathbf{a}_3}, \qquad \mathbf{b}_2 = 2\pi\frac{\mathbf{a}_3 \times \mathbf{a}_1}{\mathbf{a}_1 \cdot \mathbf{a}_2 \times \mathbf{a}_3}, \qquad \mathbf{b}_3 = 2\pi\frac{\mathbf{a}_1 \times \mathbf{a}_2}{\mathbf{a}_1 \cdot \mathbf{a}_2 \times \mathbf{a}_3} \tag{1.21}$$

such that each reciprocal vector is perpendicular to the plane formed by the lattice vectors with the other two indices. The dot product of vectors a and b is then

$$\mathbf{a}_i \cdot \mathbf{b}_j = \begin{cases} 2\pi & i = j, \\ 0 & i \neq j \end{cases} \tag{1.22}$$

Now a vector $\mathbf{G}_{hkl}$ can be defined as

$$\mathbf{G}_{hkl} = h\mathbf{b}_1 + k\mathbf{b}_2 + l\mathbf{b}_3 \tag{1.23}$$

It can be shown that $\mathbf{G}_{hkl}$ has direction normal to the hkl planes, and length

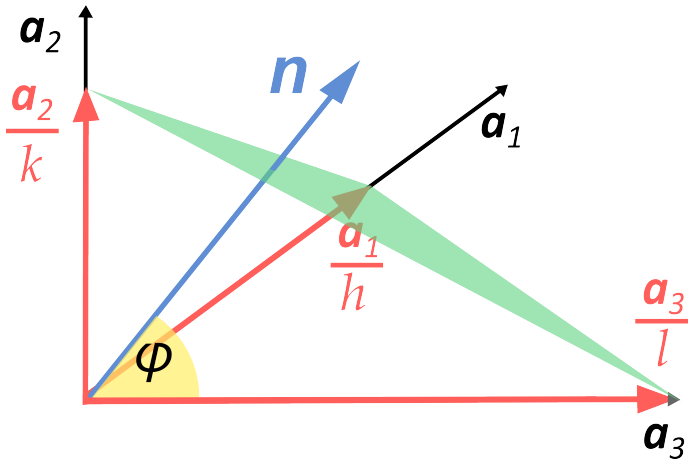

Figure 1.6: hkl plane in green with normal vector $\mathbf{n}$ making an angle φ with $\mathbf{a}_3/l$.

reciprocal to the inter-planar distance d_{hkl}. As in figure 1.6, $(\frac{\mathbf{a}_2}{k} - \frac{\mathbf{a}_3}{l})$ and $(\frac{\mathbf{a}_1}{h} - \frac{\mathbf{a}_2}{k})$ are two vectors along the hkl plane. If the dot product of $\mathbf{G}_{hkl}$ with each of these vectors is 0, orthogonality with the plane is verified.

$$(\frac{\mathbf{a}_2}{k} - \frac{\mathbf{a}_3}{l}) \cdot (h\mathbf{b}_1 + k\mathbf{b}_2 + l\mathbf{b}_3) = \frac{\mathbf{a}_2}{k}k \cdot \mathbf{b}_2 - \frac{\mathbf{a}_3}{l}l \cdot \mathbf{b}_3 = 2\pi - 2\pi = 0$$
$$(\frac{\mathbf{a}_1}{h} - \frac{\mathbf{a}_2}{k}) \cdot (h\mathbf{b}_1 + k\mathbf{b}_2 + l\mathbf{b}_3) = \frac{\mathbf{a}_1}{h}h \cdot \mathbf{b}_1 - \frac{\mathbf{a}_2}{k}k \cdot \mathbf{b}_2 = 2\pi - 2\pi = 0$$

Then the magnitude of $\mathbf{G}_{hkl}$ can be derived geometrically. From figure 1.6, the inter-planar distance d_{hkl} is as follows

$$d_{hkl} = |\frac{\mathbf{a}_3}{l}| \cos\varphi = \frac{\mathbf{a}_3}{l} \cdot \mathbf{n} \tag{1.24}$$

where $\mathbf{n}$ is the vector normal to the hkl plane making angle φ with $\mathbf{a}_3$. Since $\mathbf{G}_{hkl}$ is known to be orthogonal to hkl, we rewrite the $\mathbf{n}$ and hence the expression for d_{hkl},

$$\mathbf{n} = \frac{\mathbf{G}_{hkl}}{|\mathbf{G}_{hkl}|}$$

$$d_{hkl} = \frac{\mathbf{a}_3}{l} \cdot \frac{h\mathbf{b}_1 + k\mathbf{b}_2 + l\mathbf{b}_3}{|\mathbf{G}_{hkl}|} = \frac{2\pi}{|\mathbf{G}_{hkl}|} \tag{1.25}$$

as required. The reciprocal lattice will prove to be a useful tool as we build toward a description of scattering by a crystal. From equation 1.17, scattering amplitude of a charge element at $\mathbf{r}$ is proportional to $e^{i\Delta\mathbf{k}\cdot\mathbf{r}}$. In a crystal, the scattering amplitude must be periodic in d_{hkl}, so the scattering vector

$$\mathbf{q} = \mathbf{k} - \mathbf{k}_0 \tag{1.26}$$

has magnitude;

$$q = |\mathbf{q}| = \frac{2\pi}{d_{hkl}} \tag{1.27}$$

or simply,

$$\mathbf{q} = \Delta\mathbf{k} = \mathbf{G}_{hkl} \tag{1.28}$$

A graphical representation of this equation, the Ewald sphere, is shown in figure 1.7. By taking the dot product of $\Delta\mathbf{k}$ and $\mathbf{G}_{hkl}$ with the lattice vectors $\mathbf{a}_1\mathbf{a}_2\mathbf{a}_3$, and using equation 1.22, this can be restated as the Laue equations

$$\begin{aligned} \mathbf{q} \cdot \mathbf{a}_1 &= 2\pi h \\ \mathbf{q} \cdot \mathbf{a}_2 &= 2\pi k \\ \mathbf{q} \cdot \mathbf{a}_3 &= 2\pi l \end{aligned} \tag{1.29}$$

In a cubic unit cell with length a; the magnitude of the scattering vector, Miller indices, and lattice spacing are related by the following,

$$q = \frac{2\pi}{d_{hkl}} = 2\pi\frac{\sqrt{h^2 + k^2 + l^2}}{a} \tag{1.30}$$

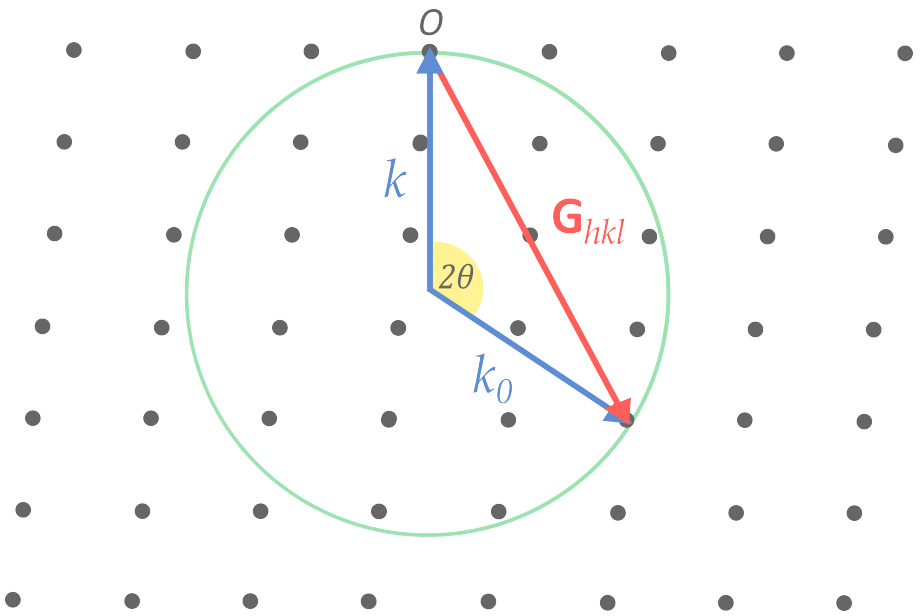

Figure 1.7: Ewald sphere construction in 2D, the diffraction condition is met where the sphere about the origin of **k** intersects with another reciprocal lattice point.

1.3 X-ray Diffraction by Crystals

This section continues from X-ray Diffraction by Warren [1], now considering the classical scattering of a monochromatic X-ray beam by a small crystal at a point of observation P some distance R from the crystal origin. Since the crystal is small, and X-ray source far away, the primary beam can be treated as a plane wave.

The phase of the electric field acting at atom n in unit cell $m_1m_2m_3$, $\mathbf{R}_m^n$ then

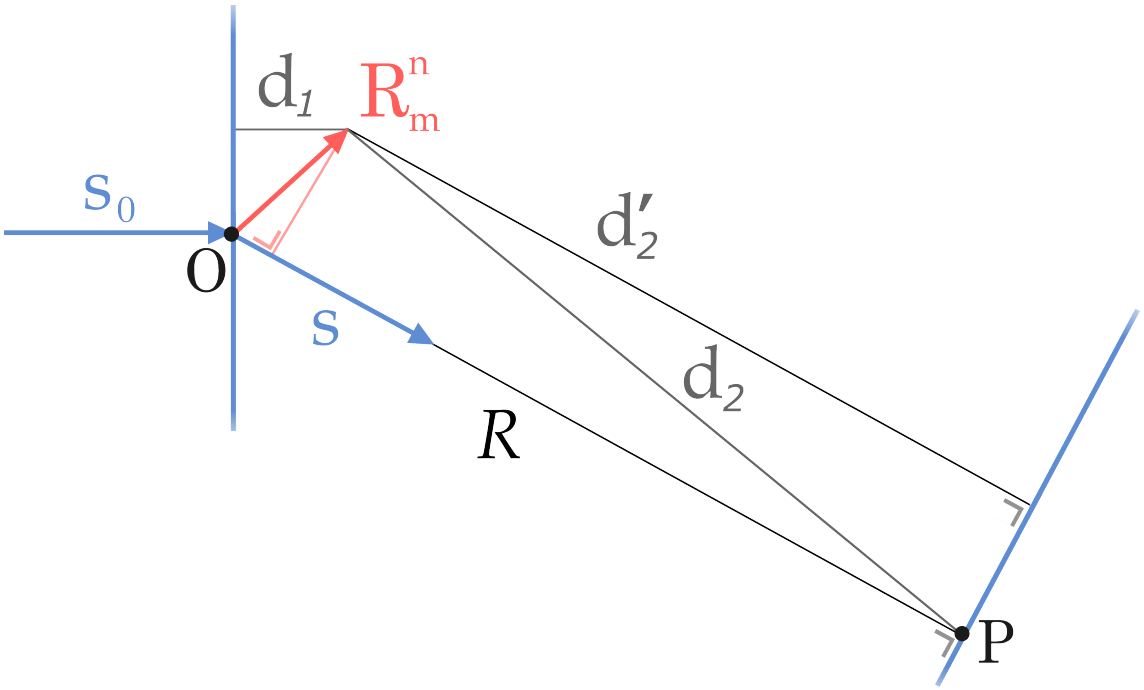

Figure 1.8: Scattering by an atom n in unit cell $m_1m_2m_3$ of a small crystal by a primary beam plane polarised perpendicular to the paper, as measured by an observer at P some distance R from the crystal origin.

depends on d_1, shown in figure 1.8. Following from equation 1.16, the instantaneous electric field at P due to classical scattering from atom n is given by the following,

$$\epsilon_P = \frac{E_0 e^2}{4\pi\epsilon_0 m_e c^2 R} f_n \cos(\omega t - k(d_1 + d_2)) \tag{1.31}$$

Since the crystal is also small with respect to R, the scattered beam can also be treated with the plane wave approximation such that $d_1 + d_2 \to d_1 + d_2'$. Rewriting in terms of $\mathbf{s}$, $\mathbf{s}_0$, and $\mathbf{R}_m^n$,

$$\begin{aligned} d_2' &= R - \mathbf{R}_m^n \cdot \mathbf{s} \\ d_1 &= \mathbf{R}_m^n \cdot \mathbf{s}_0 \\ d_1 + d_2 &= R - \mathbf{R}_m^n \cdot \mathbf{s} + \mathbf{R}_m^n \cdot \mathbf{s}_0 \\ &= R - \mathbf{R}_m^n \cdot (\mathbf{s} - \mathbf{s}_0) \end{aligned}$$

The instantaneous field at P due to atom n in unit cell $m_1m_2m_3$ at $\mathbf{R}_m^n$ is then

$$\epsilon_P = \frac{E_0 e^2}{4\pi\epsilon_0 m_e c^2 R} f_n \cos(\omega t - k(R - \mathbf{R}_m^n \cdot (\mathbf{s} - \mathbf{s}_0))) \tag{1.32}$$

In exponential form

$$\epsilon_P = \frac{E_0 e^2}{4\pi\epsilon_0 m_e c^2 R} f_n e^{(i\omega t - ik(R - \mathbf{R}_m^n \cdot (\mathbf{s}-\mathbf{s}_0)))}$$

with

$$e^{(i\omega t - ik(R - \mathbf{R}_m^n \cdot (\mathbf{s}-\mathbf{s}_0)))} = e^{(i\omega t - ikR + ik\mathbf{R}_m^n \cdot (\mathbf{s}-\mathbf{s}_0))} = e^{i(\omega t - kR)} e^{ik\mathbf{R}_m^n \cdot (\mathbf{s}-\mathbf{s}_0))}$$

The total field at P is found by summing over all n atoms in all unit cells. Assuming the crystal is a parallelepiped with dimensions $N_1\mathbf{a}_1 \times N_2\mathbf{a}_2 \times N_3\mathbf{a}_3$, and separating into 4 summations

$$\epsilon_P = \frac{E_0 e^2}{4\pi\epsilon_0 m_e c^2 R} e^{i(\omega t - kR)} \sum_n f_n e^{-ik(\mathbf{s}-\mathbf{s}_0)\cdot \mathbf{r}_n} \tag{1.33}$$

$$\times \sum_{m_1=0}^{N_1-1} e^{-ik(\mathbf{s}-\mathbf{s}_0)\cdot m_1\mathbf{a}_1} \sum_{m_2=0}^{N_2-1} e^{-ik(\mathbf{s}-\mathbf{s}_0)\cdot m_2\mathbf{a}_2} \sum_{m_3=0}^{N_3-1} e^{-ik(\mathbf{s}-\mathbf{s}_0)\cdot m_3\mathbf{a}_3}$$

The first summation is known as the structure factor, F, this term defines the scattering intensity contribution from atomic positions within the unit cell.

Each of the latter 3 terms are sums of geometric progressions $a + ar + ar^2 + ... + l$, where r is the common ratio between consecutive terms. This has a well-known solution, $\frac{rl-a}{r-1}$, as such the above can be simplified

$$\epsilon_P = \frac{E_0 e^2}{4\pi\epsilon_0 m_e c^2 R} e^{i(\omega t - kR)} F \frac{e^{ik(\mathbf{s}-\mathbf{s}_0)\cdot N_1\mathbf{a}_1} - 1}{e^{ik(\mathbf{s}-\mathbf{s}_0)\cdot \mathbf{a}_1} - 1} \frac{e^{ik(\mathbf{s}-\mathbf{s}_0)\cdot N_2\mathbf{a}_2} - 1}{e^{ik(\mathbf{s}-\mathbf{s}_0)\cdot \mathbf{a}_2} - 1} \frac{e^{ik(\mathbf{s}-\mathbf{s}_0)\cdot N_3\mathbf{a}_3} - 1}{e^{ik(\mathbf{s}-\mathbf{s}_0)\cdot \mathbf{a}_3 - 1}} \tag{1.34}$$

Recalling $E^2 = \epsilon^*\epsilon$, this product produces terms of the form

$$(\frac{e^{iNx} - 1}{e^{ix} - 1})(\frac{e^{-iNx} - 1}{e^{-ix} - 1}) = \frac{1 + 1 - e^{iNx} - e^{-iNx}}{1 + 1 - e^{ix} - e^{-ix}} = \frac{2 - 2\cos(Nx)}{2 - 2\cos(x)}$$

where $x = ik(\mathbf{s} - \mathbf{s}_0) \cdot a_i$. Using the identity

$$\sin^2\theta = \frac{1}{2}(1 - \cos(2\theta))$$

$$4\sin^2\theta = 2 - 2\cos(2\theta)$$

Hence,

$$E^2 \propto F^* F \frac{\sin^2[(\frac{k}{2})(\mathbf{s} - \mathbf{s}_0) \cdot N_1\mathbf{a}_1]}{\sin^2[(\frac{k}{2})(\mathbf{s} - \mathbf{s}_0) \cdot \mathbf{a}_1]} \frac{\sin^2[(\frac{k}{2})(\mathbf{s} - \mathbf{s}_0) \cdot N_2\mathbf{a}_2]}{\sin^2[(\frac{k}{2})(\mathbf{s} - \mathbf{s}_0) \cdot \mathbf{a}_2]} \frac{\sin^2[(\frac{k}{2})(\mathbf{s} - \mathbf{s}_0) \cdot N_3\mathbf{a}_3]}{\sin^2[(\frac{k}{2})(\mathbf{s} - \mathbf{s}_0) \cdot \mathbf{a}_3]} \tag{1.35}$$

In practice, atoms in a crystal oscillate about their average positions due to thermal vibrations. This attenuates the scattering amplitude by the Debye-Waller factor $e^{-M} = e^{-8\pi^2\langle u^2\rangle sin^2\theta/\lambda^2}$ where u is the component of instantaneous thermal displacement along $\mathbf{s} - \mathbf{s}_0$. Including this term in a temperature-modified structure factor,

$$F_T^2 = \sum_n f_n e^{-ik(\mathbf{s}-\mathbf{s}_0)\cdot \mathbf{r}_n} \sum_n f_n e^{ik(\mathbf{s}-\mathbf{s}_0)\cdot \mathbf{r}_n} \tag{1.36}$$

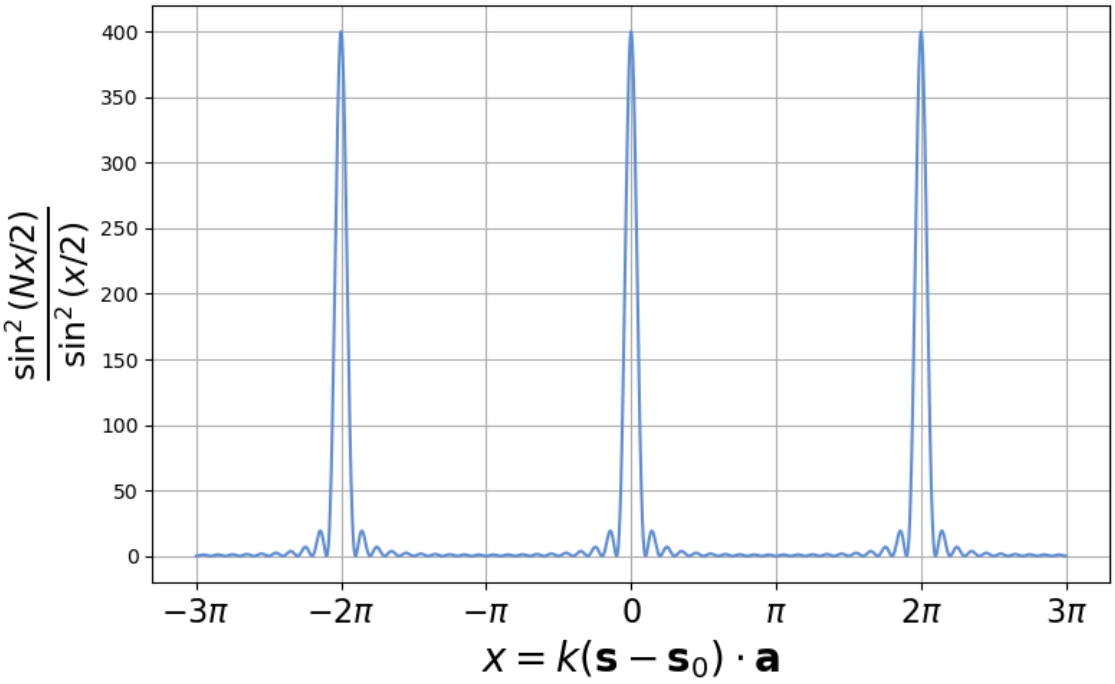

Figure 1.9: $\frac{\sin^2(Nx/2)}{\sin^2(x/2)}$ as a function of x for $N = 20$, sharp maxima appear where x is an integer multiple of 2π.

As in equation 1.7, a polarisation factor is introduced by taking the average value of E^2 at P. For a horizontally polarised primary beam with intensity I_0, the diffracted intensity from a small parallelepiped crystal is

$$I_p = I_e F_T^2 \frac{\sin^2[(\frac{k}{2})(\mathbf{s}-\mathbf{s}_0)\cdot N_1\mathbf{a}_1]}{\sin^2[(\frac{k}{2})(\mathbf{s}-\mathbf{s}_0)\cdot \mathbf{a}_1]} \frac{\sin^2[(\frac{k}{2})(\mathbf{s}-\mathbf{s}_0)\cdot N_2\mathbf{a}_2]}{\sin^2[(\frac{k}{2})(\mathbf{s}-\mathbf{s}_0)\cdot \mathbf{a}_2]} s \frac{\sin^2[(\frac{k}{2})(\mathbf{s}-\mathbf{s}_0)\cdot N_3\mathbf{a}_3]}{\sin^2[(\frac{k}{2})(\mathbf{s}-\mathbf{s}_0)\cdot \mathbf{a}_3]} \tag{1.37}$$

where I_e is defined as follows,

$$I_e = I_0 \frac{e^4}{16\pi^2\epsilon_0^2 m_e^2 c^4 R^2}(\cos^2\Phi) \tag{1.38}$$

The intensity of the diffracted beam is sharply dependent on the three quotients above as in figure 1.9. The maxima of the quotients occur at

$$\frac{k}{2}(\mathbf{s}-\mathbf{s}_0)\cdot a_i = n\pi$$
$$\mathbf{q}\cdot a_i = 2n\pi$$

which are simply the Laue equations, as in 1.29. The structure factor F for which Bragg's law is satisfied can hence be written in terms of $\mathbf{G}_{hkl}$ and unit cell vectors $\mathbf{r}_n$,

$$F_{hkl} = \sum_n f_n e^{i\mathbf{q}\cdot\mathbf{r}_n} = \sum_n f_n e^{i\mathbf{G}_{hkl}\cdot(x_n\mathbf{a}_1 + y_n\mathbf{a}_2 + z_n\mathbf{a}_3)} \tag{1.39}$$

Using equations 1.23 and 1.22, the structure factor for a hkl reflection becomes

$$F_{hkl} = \sum_n f_n e^{2\pi i(hx_n + ky_n + lz_n)} \tag{1.40}$$

Since the intensity of a Bragg reflection for a certain hkl vanishes where the structure

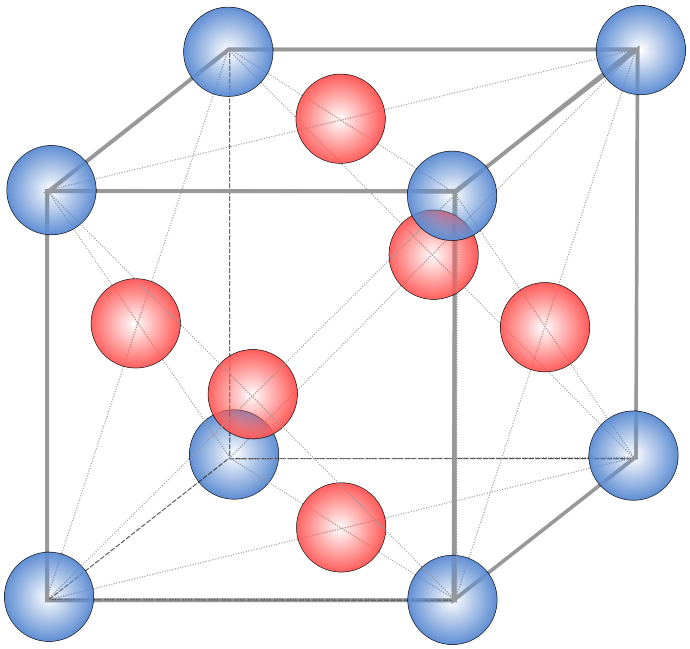

Figure 1.10: Face-centred cubic (FCC) unit cell with blue atoms positioned on its corners, and red atoms on its faces.

factor is zero, the underlying Bravais lattice can be identified. Shown in figure 1.10 is the unit cell of a crystal with a face-centred cubic (FCC) Bravais lattice. The unit cell contains 4 atoms at positions $(0,0,0)$, $(\frac{1}{2},\frac{1}{2},0)$, $(\frac{1}{2},0,\frac{1}{2})$, $(0,\frac{1}{2},\frac{1}{2})$ in terms of the unit cell length a. The crystal structure is then identical under the following translations

$$\begin{aligned} x_n, y_n, z_n &\to x_n + \frac{1}{2}, y_n + \frac{1}{2}, z_n \\ x_n, y_n, z_n &\to x_n + \frac{1}{2}, y_n, z_n + \frac{1}{2} \\ x_n, y_n, z_n &\to x_n, y_n + \frac{1}{2}, z_n + \frac{1}{2} \end{aligned}$$

Expressing the structure factor as a sum over such a group of 4 identical atoms

$$\begin{aligned} F_{hkl} = \sum_{n/4} f_n \Big\{ & e^{2\pi i(hx_n + ky_n + lz_n)} + e^{2\pi i\left[h(x_n+\frac{1}{2}) + k(y_n+\frac{1}{2}) + lz_n\right]} \\ & + e^{2\pi i\left[h(x_n+\frac{1}{2}) + ky_n + l(z_n+\frac{1}{2})\right]} + e^{2\pi i\left[hx_n + k(y_n+\frac{1}{2}) + l(z_n+\frac{1}{2})\right]} \end{aligned} \tag{1.41}$$

which simplifies to

$$F_{hkl} = \left[1 + e^{\pi i(h+k)} + e^{\pi i(h+l)} + e^{\pi i(k+l)}\right] \sum_{n/4} f_n e^{2\pi i(hx_n + ky_n + lz_n)} \tag{1.42}$$

and since $e^{\pi i m} = (-1)^m$, the structure factor vanishes for mixed even and odd values of hkl and becomes

$$4 \sum_{n/4} f_n e^{2\pi i(hx_n + ky_n + lz_n)} \tag{1.43}$$

for all even or all odd hkl.

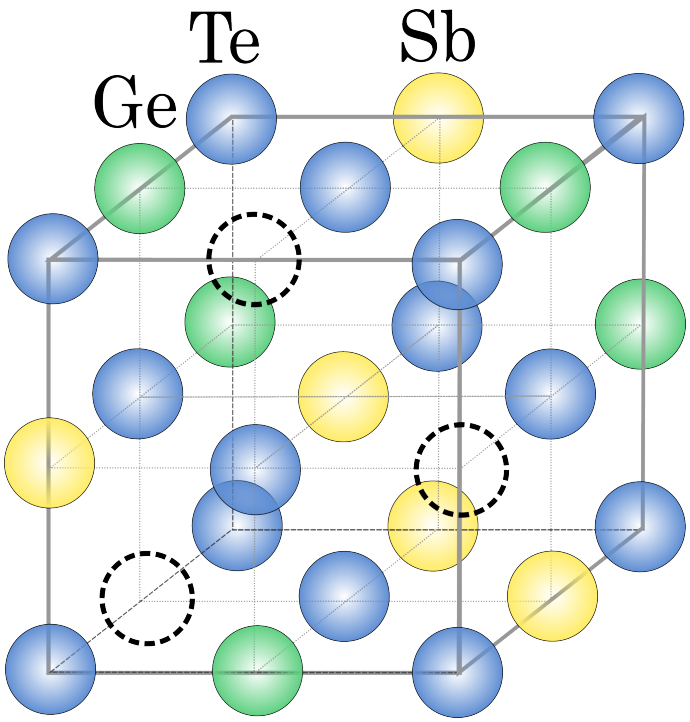

Figure 1.11: Unit cell of rock-salt GST consisting of an FCC tellurium sublattice, and interpenetrating FCC sublattice of germanium, antimony, and vacancies.

The rock salt configuration of $Ge_2Sb_2Te_5$ consists of two interpenetrating FCC sublattices; an anion sublattice is occupied by Te, and a cation sublattice occupied by Ge (40%), Sb (40%), and vacancies (20%). The cubic cell contains 4 Te at the FCC lattice positions as above, and 4 Ge/Sb/vacancies at $(\frac{1}{2}, \frac{1}{2}, \frac{1}{2}), (0, 0, \frac{1}{2}), (0, \frac{1}{2}, 0), (\frac{1}{2}, 0, 0)$. The structure factor can be written as the sum of the two lattice contributions

$$F_{hkl} = \sum_{\text{Te}} f_{\text{Te}} e^{2\pi i(hx_n + ky_n + lz_n)} + \sum_{\text{cat}} f_{\text{cat}} e^{2\pi i(hx_n + ky_n + lz_n)} \tag{1.44}$$

where the average scattering factor for the cation sublattice is

$$f_{\text{cat}} = 0.4 f_{\text{Ge}} + 0.4 f_{\text{Sb}} \tag{1.45}$$

Using 1.43, and positions $(0, 0, 0)$ for Te, and $(\frac{1}{2}, \frac{1}{2}, \frac{1}{2})$ for Ge/Sb, for unmixed hkl

$$F_{hkl} = 4 f_{\text{Te}} + 4[0.4 f_{\text{Ge}} + 0.4 f_{\text{Sb}}] e^{\pi i(h+k+l)} \tag{1.46}$$

if hkl are all even,

$$F_{hkl} = 4 f_{\text{Te}} + 1.6 f_{\text{Ge}} + 1.6 f_{\text{Sb}} \tag{1.47}$$

if hkl are all odd,

$$F_{hkl} = 4f_{\mathrm{Te}} - 1.6f_{\mathrm{Ge}} - 1.6f_{\mathrm{Sb}} \tag{1.48}$$

and for mixed even and odd hkl values

$$F_{hkl} = 0 \tag{1.49}$$

Due to the finite width of the peaks in figure 1.9, some diffracted intensity comes from $\mathbf{q}$ differing slightly from $\mathbf{G}_{hkl}$. The observable quantity will therefore be an integrated intensity over an angular range close to the Bragg angle. Letting $\mathbf{q} = \mathbf{G}_{hkl} + \Delta\mathbf{q}$, and rewriting the $\sin^2$ terms in equation 1.37 in terms of $\Delta\mathbf{q}$,

$$\begin{aligned}\sin^2(\pi/\lambda)(\mathbf{s}-\mathbf{s}_0)\cdot N_1\mathbf{a}_1 = \sin^2\frac{(\mathbf{k}-\mathbf{k}_0)}{2}\cdot N_1\mathbf{a}_1 \rightarrow \sin^2(\frac{1}{2}\mathbf{G}_{hkl}+\frac{1}{2}\Delta\mathbf{q})\cdot N_1\mathbf{a}_1 \\ = \sin^2(\pi h N_1 + \frac{1}{2}\Delta\mathbf{q}\cdot N_1\mathbf{a}_1) \\ = \sin^2(\frac{1}{2}\Delta\mathbf{q}\cdot N_1\mathbf{a}_1)\end{aligned}$$

Writing $\Delta\mathbf{q}$ in terms of the reciprocal lattice vectors,

$$\Delta\mathbf{q} = (p_1\mathbf{b}_1 + p_2\mathbf{b}_2 + p_3\mathbf{b}_3) \tag{1.50}$$

Using equation 1.22,

$$\sin^2(\frac{1}{2}\Delta\mathbf{q}\cdot N_1\mathbf{a}_1) = \sin^2(\pi N_1 p_1) \tag{1.51}$$

The intensity at point of observation P can hence be expressed as

$$I_p = I_e F_T F_T^* \frac{\sin^2(\pi N_1 p_1)}{\sin^2(\pi p_1)}\frac{\sin^2(\pi N_2 p_2)}{\sin^2(\pi p_2)}\frac{\sin^2(\pi N_3 p_3)}{\sin^2(\pi p_3)} \tag{1.52}$$

Since Bragg's Law is satisfied only for $p_1p_2p_3$ close to zero, the denominators can be further simplified as

$$I_p = I_e F_T F_T^* \frac{\sin^2(\pi N_1 p_1)}{(\pi p_1)^2}\frac{\sin^2(\pi N_2 p_2)}{(\pi p_2)^2}\frac{\sin^2(\pi N_3 p_3)}{(\pi p_3)^2} \tag{1.53}$$

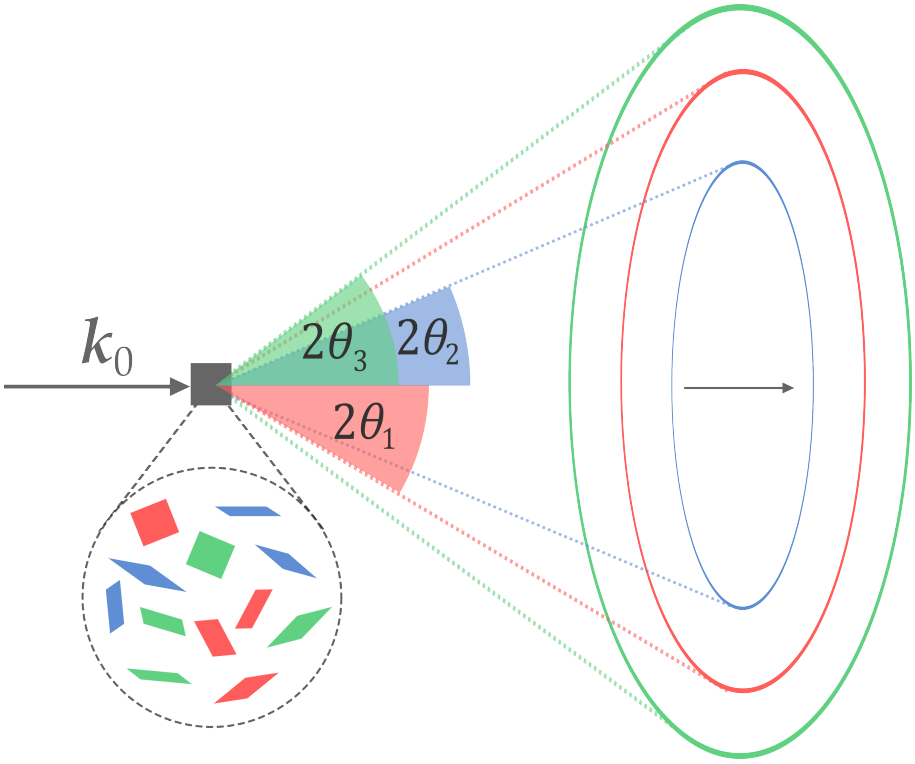

Figure 1.12: Diffraction by small crystals in a powder, each set of planes hkl will be oriented at the correct Bragg angle in some of the crystals, forming elements of diffraction rings for each d_{hkl}.

In this work, powder samples of GST are used, these contain large numbers of small GST crystals with random orientations. When a monochromatic beam is incident on a powder sample, there will always be some crystals with hkl planes at the correct angle to allow the corresponding Bragg reflection. As the diffracted beam makes an angle $2\theta_{hkl}$ with the primary beam, the radiation from the small crystals at random orientations create elements of a cone for each plane spacing d_{hkl} with half apex angle $2\theta_{hkl}$ as illustrated in figure 1.12.

Each set of hkl planes in each crystal makes some angle $\theta_{hkl} + \alpha$ with the primary beam, each with a normal vector $\mathbf{G}_{hkl}$. The number of normal vectors is a product between the number of crystals in the sample M, and the hkl multiplicity m_{hkl}. The latter term accounts for different hkl planes having identical spacing d_{hkl} and structure factor. This emerges from the symmetry of the crystal.

The termini of the Mm_{hkl} normal vectors are uniformly distributed on a sphere of radius $|\mathbf{G}_{hkl}| = \frac{2\pi}{d_{hkl}}$ and surface area $4\pi(\frac{2\pi}{d_{hkl}})^2$ as in figure 1.13. The number of crystals with a hkl plane at an angle between $\theta_{hkl}+\alpha$ and $\theta_{hkl}+\alpha+d\alpha$ with respect to the primary beam is

$$dM = \frac{Mm_{hkl}}{4\pi(\frac{2\pi}{d_{hkl}})^2} 2\pi(\frac{2\pi}{d_{hkl}})^2 \cos(\theta+\alpha)d\alpha \tag{1.54}$$

with $2\pi(\frac{2\pi}{d_{hkl}})^2 \cos(\theta+\alpha)d\alpha$ being the area of a narrow ring on a sphere. The Bragg

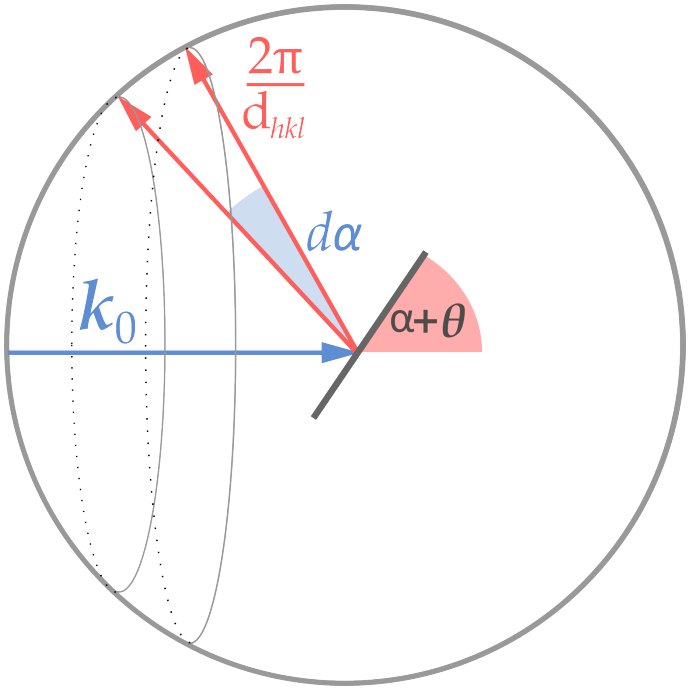

Figure 1.13: Sphere of radius $\frac{2\pi}{d_{hkl}}$ containing termini of normal vectors to hkl planes in a powder sample. A narrow ring on the sphere is traced out by hkl reflections from planes angled between $\theta_{hkl} + \alpha$ and $\theta_{hkl} + \alpha + d\alpha$ with the primary beam.

condition is satisfied where $\alpha \approx 0$,

$$dM = \frac{Mm_{hkl}}{2} \cos(\theta) d\alpha \tag{1.55}$$

The area element on the receiving receiving surface is given by $dA = R^2 d\beta d\gamma$ where β and γ are the angular coordinates on the receiving surface measured relative to the diffracted beam, with β lying in the scattering plane and γ perpendicular to it. The total diffracted power is the product between the single crystal intensity and number of crystals integrated over the detector area,

$$P = \iiint I_p \frac{Mm_{hkl}}{2} \cos(\theta) R^2 d\alpha d\beta d\gamma \tag{1.56}$$

The intensity I_p is expressed in terms of the reciprocal space variables $p_1 p_2 p_3$. To express the above as a volume integral in reciprocal space, the volume element traced by $\Delta\mathbf{q}$ in reciprocal space when $d\alpha d\beta d\gamma$ are changed is as follows,

$$dV = d(\Delta\mathbf{q})_\beta \cdot d(\Delta\mathbf{q})_\gamma \times d(\Delta\mathbf{q})_\alpha = \sin 2\theta d\alpha d\beta d\gamma$$

as the angle between reciprocal-space displacement vectors $d(\Delta\mathbf{q})_\beta$ and $d(\Delta\mathbf{q})_\gamma$ subtends the scattering angle 2θ in reciprocal space. In terms of $p_1 p_2 p_3$ where v_a is the unit cell volume, and is related to the reciprocal unit cell volume by $v_b = \frac{(2\pi)^3}{v_a}$

$$d(\Delta\mathbf{q}) = (dp_1 \mathbf{b}_1 + dp_2 \mathbf{b}_2 + dp_3 \mathbf{b}_3)$$

$$dV = \mathbf{b}_1 dp_1 \cdot \mathbf{b}_2 dp_2 \times \mathbf{b}_3 dp_3 = v_b dp_1 dp_2 dp_3 = \frac{(2\pi)^3}{v_a} dp_1 dp_2 dp_3$$

The total diffracted power becomes

$$P = I_e \frac{M m_{hkl} F_T F_T^* 2\pi^3}{v_a \sin\theta} \int_{-\infty}^{\infty} \frac{\sin^2(\pi N_1 p_1)}{(\pi p_1)^2} dp_1 \int_{-\infty}^{\infty} \frac{\sin^2(\pi N_2 p_2)}{(\pi p_2)^2} dp_2 \times \int_{-\infty}^{\infty} \frac{\sin^2(\pi N_3 p_3)}{(\pi p_3)^2} dp_3 \tag{1.57}$$

Power per unit length of the diffraction ring on detector at a distance R from the sample is

$$P' = \frac{P}{2\pi R \sin 2\theta} \tag{1.58}$$

Intensity between the diffraction rings on the receiving surface is due to deviations from the ideal periodic crystal structure. This diffuse scattering data can be used to determine crystal properties outside of the structure of its average unit cell. This can include thermal lattice vibrations, vacancy/substitutional defects, and faults. Essentially, anything that disrupts the local order in a crystal will act to decrease the amplitude of Bragg peaks, and create diffuse scattering [34].

Chapter 2

Experimental Methods

2.1 Time resolved X-ray Diffraction

By pumping a sample with an optical pulse, and probing with an X-ray pulse, structural dynamics can be induced and mapped in crystalline materials. By sorting the resultant diffraction patterns by delay between the pulses, real-time structural dynamics can be reconstructed. Using femtosecond pulses, this can be achieved on the timescale of atomic motions [35].

2.1.1 FemtoMAX Overview

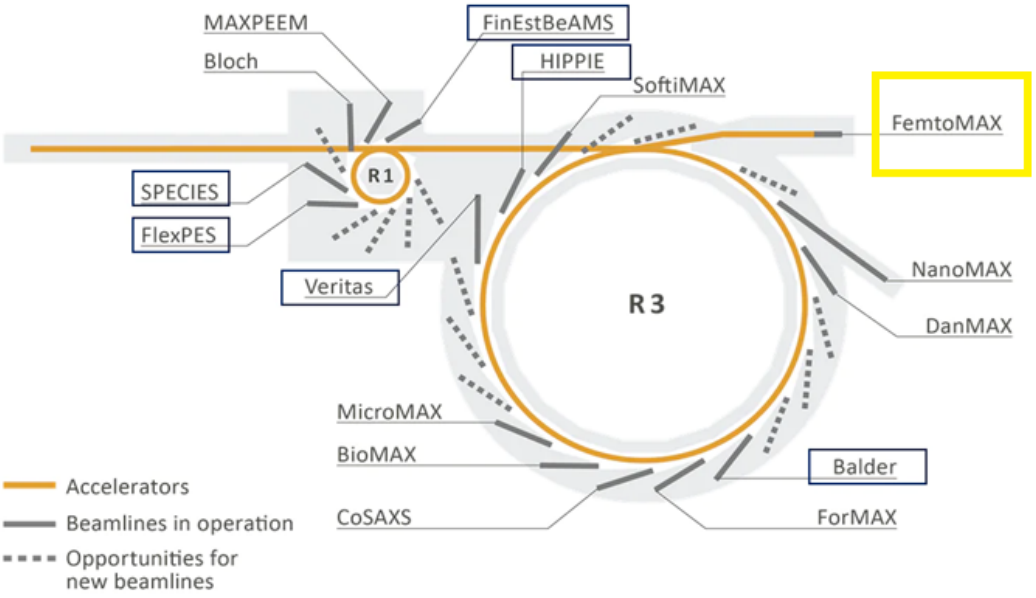

Figure 2.1: MAX IV overview with FemtoMAX at the short pulse facility (SPF) highlighted by the yellow box. Image credit: MAX IV Laboratory.

The FemtoMAX beamline at MAX IV Laboratory is dedicated to investigating structural dynamics at femtosecond timescales. Electron bunches from the MAX

IV linear accelerator (LINAC) with <100 fs duration are sent through a 10 m undulator, the accelerated electrons emit fs X-ray pulses with energies in the 1.85-20 keV range. A dipole magnet then bends the electrons onto a beam dump, and an adjustable slit defines the X-ray beam which propagates the experimental hutch.

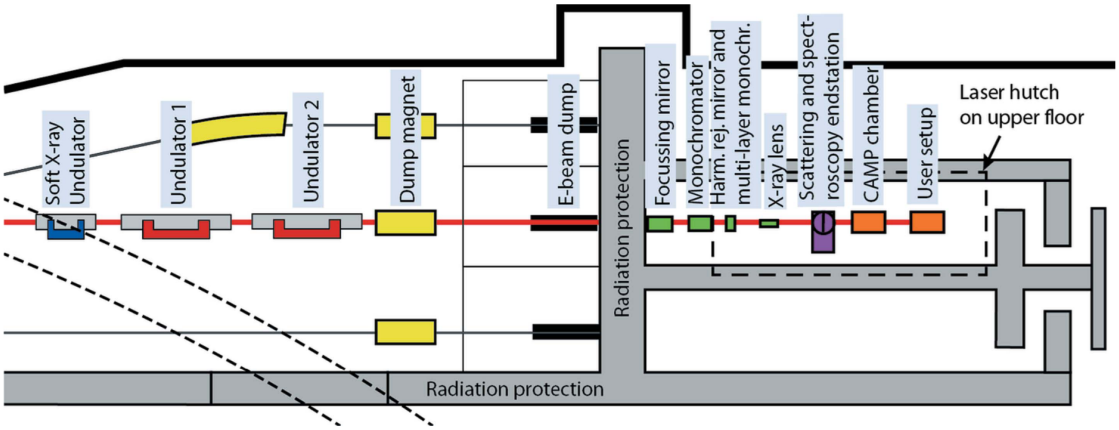

Figure 2.2: Top-down overview of X-ray generation and optics at FemtoMAX. Image from Enquist et. al. [29].

The X-ray radiation produced by the undulator contains both the fundamental energy defined by the undulator period, and harmonics. To select only the desired X-ray energy, a multi-layer monochromator (MLM) is used. Each strip on the MLM consists of many alternating layers of two materials. This creates a crystal-like periodic structure where the thickness d of each pair of layers defined the Bragg condition for an wave incident at an angle θ,

$$n\lambda = 2d \sin\theta \tag{2.1}$$

X-rays with wavelength λ are reflected. Two such multi-layer mirrors are oriented such that the outgoing and incoming beams are parallel. Each multilayer mirror at FemtoMAX has three stripes of different material pairs, corresponding to different energy ranges.

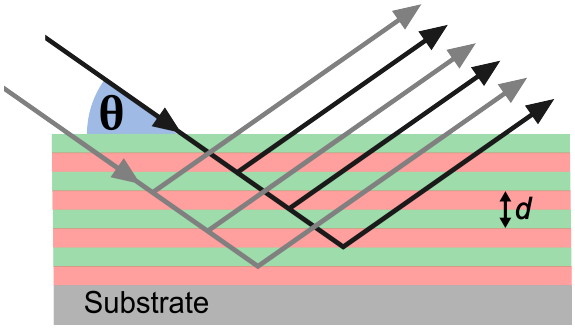

Figure 2.3: Workings of a stripe on the multi-layer monochromator. Different layer thicknesses d can be used to select for different λ.

An additional pair of stripes on the same substrate are the harmonic rejection mirrors, used to reject higher order harmonics. Higher energy X-rays require a more grazing angle to be reflected than those with lower energy. Therefore, by placing a mirror close to the critical angle of the desired harmonic, the higher energy radiation is not reflected. The X-ray beam from the undulator is focused by a bendable cylindrical mirror. Further lens stacks can be used to optimised the beam as required [29].

A femtosecond Ti:sapphire laser (KM Laboratories Red Wyvern) is housed in a dedicated laser hutch on the upper floor. The laser provides 800 nm optical pump pulses for pump–probe experiments, and an optical parametric amplifier (OPA) can be used to generate 1100-2600 nm pulses [36]. The laser is synchronised to the LINAC using dedicated timing diagnostics. Motorised delay stages are used shorten/lengthen the laser path, and therefore scan over some interval of pump-probe delays.

2.1.2 Timing tools at FemtoMAX

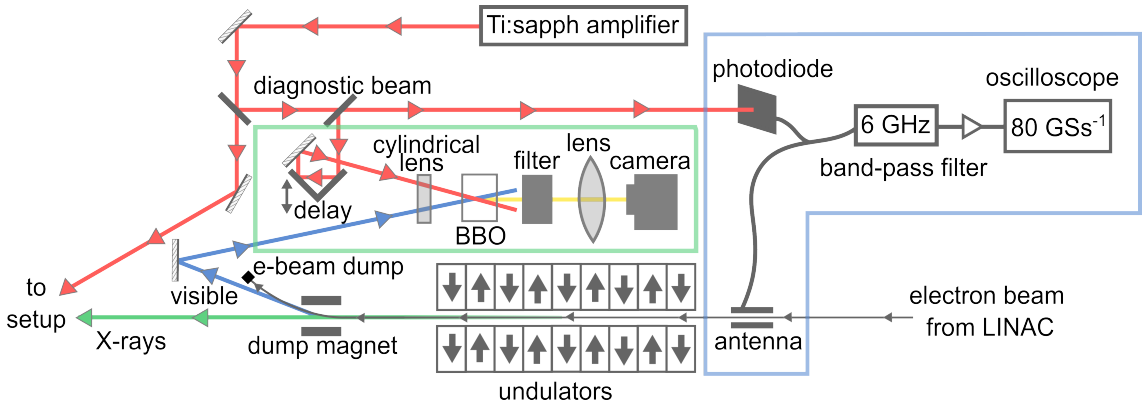

Figure 2.4: Schematic of the timing tools used to measure timing jitter at FemtoMAX. In the blue box, the 'ping' timing monitor uses the ringing of an RF cavity excited by RF pulses from the laser beam and electron bunch. The resultant signal is sampled by the oscilloscope, from which the relative timing between the pulses can be extracted. In the green box, the cross-correlator-based timing monitor uses visible light from the bending magnet, and laser light from the diagnostic beam to induce an SFG signal from a nonlinear crystal. The position of the SFG signal on the CMOS camera is dependent on the timing delay between the beams.

Of particular interest in this work are the timing tools at FemtoMAX used to measure pump-probe delay. The 'ping' timing monitor compares the delay between radio-frequency (RF) electronic signals derived from the laser pulse and electron bunch, shown in the blue box in figure 2.4. The electron bunch passing the button antenna induces a short RF pulse, and a small part of the laser beam used for diagnostics is diverted to a fast photodiode. These signals are combined using an RF combiner.

The signals then excite a 6 GHz RF cavity band-pass filter which rings for about 10 ns. This produces a waveform whose phase depends on the relative arrival time of

the two RF pulses. The signal is passed through an amplifier before being sampled by an oscilloscope at 80×10^9 samples per second. A Hilbert-transform algorithm extracts the relative phase, and hence the delay between the two signals can be determined with an accuracy of 200 fs (FWHM) [29]. In reality, two sets of photodiodes, and button antennae are used in parallel, and the resulting pump-probe delays are averaged to reduce measurement error.

The cross-correlator-based timing tool also uses part of the the diagnostic laser beam, as well as visible light extracted from the dump magnet of the LINAC. The beams are vertically focused using a cylindrical lens, and spatially overlapped in the interaction region of a beta barium borate (BBO) crystal. The position where the peaks of the pulses intersect is dependent on the timing delay. The position on a CMOS camera (Zyla 5.5M from Andor) of the sum-frequency generated (SFG) signal can therefore be used to determine the delay between the pump and probe pulses with a timing error of <30 fs during the few ps window when both overlap in the BBO [33]. The timing delay measured by the ping timing monitor is used to calibrate the relationship between pixel position on the Zyla camera and pump-probe delay.

These methods measure jitter, the fluctuations in arrival time between the pump and probe pulses. To determine the time-zero, or time when the pulses arrive simultaneously, a standardised sample is needed. To create a narrow time-zero window, this sample should have a fast response when the pump and probe beams are spatially and temporally overlapped. We used the FemtoMAX beamline to study powder samples of rock-salt GST as a candidate for this purpose.

2.2 Experiments on GST

In our experiments, powder samples of both stoichiometric $Ge_2Sb_2Te_5$, and germanium enriched GST were used, each on a silicon substrate. Each sample was mounted on a sample holder at grazing incidence ($\sim 1°$) with the X-ray beam. The pump and probe beams were spatially overlapped on the sample, and timed up to within a few ps using the ping timing monitor. The cross-correlator-based timing monitor could then be used to precisely measure jitter throughout the experiment. The diffracted X-rays are imaged by a Pilatus3 1.2M detector for each probe pulse. The pump-probe delay was varied using a delay stage. Each image therefore corresponds to a particular shot where a pump and probe beam were incident on the sample with some delay.

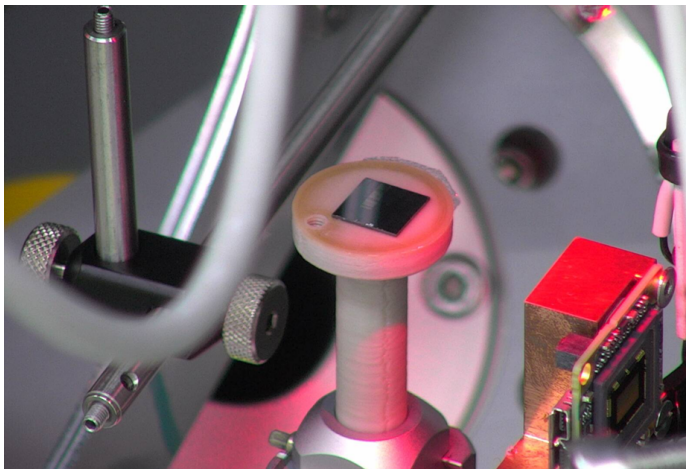

Figure 2.5: GST sample mounted on sample holder at FemtoMAX

The data presented in this work comes from three experimental runs which took place in January, March, and May 2026. In these experiments, a 1500 nm OPA beam was used to pump the sample, and an 8 keV X-ray beam was used as the probe. The parameters of these beams fluctuated depending on the state of the LINAC, and use/alignment of optics. During our second run, we had a 50 fs X-ray

Table 2.1: Experimental conditions for each of the three pump-probe measurement campaigns.

Beam Parameter	Run 1	Run 2	Run 3
X-ray flux (photons/pulse)	3.2×10^6	1.2×10^6	2×10^6
X-ray beam size (μm × μm, FWHM)	65 × 14	69×20	66×20
Max laser fluence (mJ cm^{-2})	38	39	45

pulse, allowing for our highest temporal resolution. The first 2 runs were in-air, and the third in vacuum. The diffraction pattern was imaged as a function of delay with varying laser fluence, incidence angle, and temperature. The quality of spatial overlap, and integrity of the sample also varied throughout the experiments.

Chapter 3

Analytical Methods

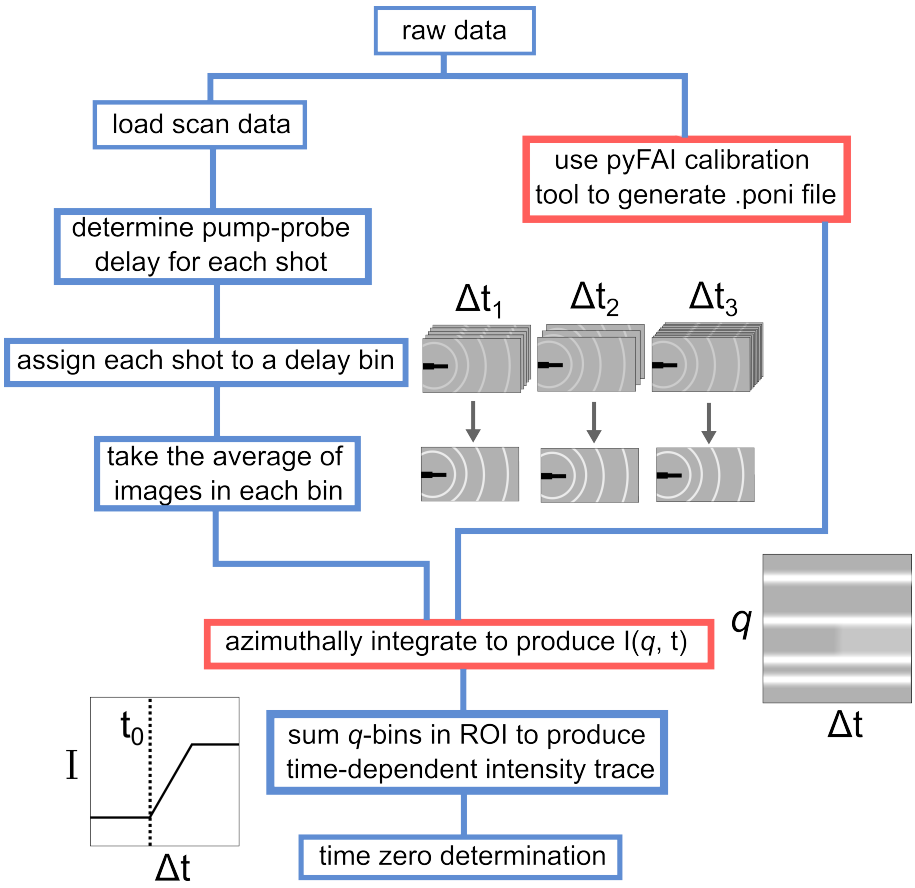

Figure 3.1: Analysis pipeline flowchart, the steps in blue were done using custom built python software, the steps in red were done with the help of existing tools from pyFAI.

The raw data for each scan over pump-probe delay is saved in a `.h5` file [37]. Hundreds to thousands of shots are contained in each scan, with typically 10's of shots per delay motor position. For each shot, there is;

1. a 2D X-ray diffraction image from the Pilatus detector
2. an RF-timing tool delay value (s)

3. delay motor position (mm)

4. a 2D image of the cross-correlator signal from the Zyla camera

There is also other information such as time of day, command line prompt for the scan, and positions of the many motors used for sample/beam alignment. These images need to be sorted and binned according to pump-probe delay given the timing information. The following analysis was implemented using Python.

3.1 Post-sorting

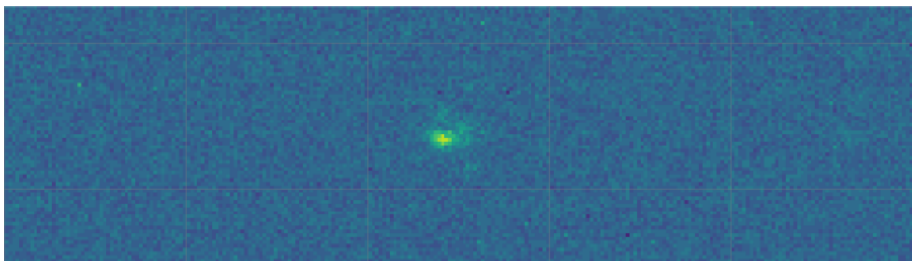

Figure 3.2: Partial camera image showing the cross-correlator signal. The x-pixel position of the signal peak is dependent on pump-probe delay.

A typical camera image of the cross-correlator signal is shown in figure 3.2. To determine the pump-probe timing delay for each shot, we use the following procedure. Firstly, we image the constant background from the Zyla camera. This is then subtracted from each of the cross-correlator images. Next, we sum the rows in each image to create a 1D lineout relating intensity to pixel column. We define window about the column with highest intensity, and use the `centroid` tool from scikit-image [38] to find the weighted centre of the beam. As some peaks are due to random γ-rays and cosmic rays, we perform a Gaussian fit to filter out shots which have peaks of small width. This can also be used to filter images with low peak intensity due to a lack of signal.

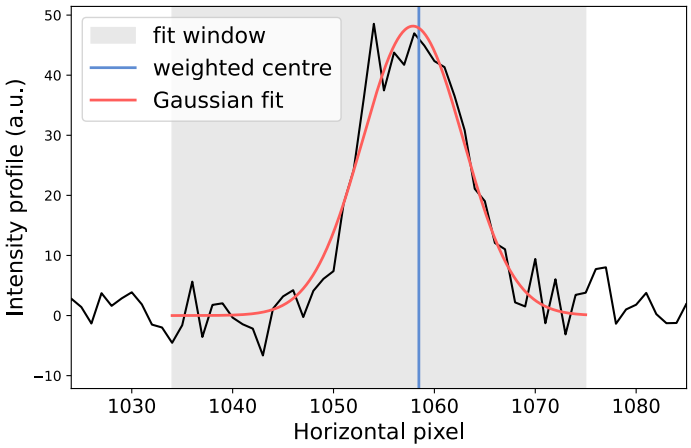

Figure 3.3: Vertical lineout of cross-correlator beam image for a single shot. The weighted centre of the peak is used to determine pump-probe delay, and the Gaussian fit is used for filtering unwanted shots.

We then plot the x-pixel position of the peak against the RF-timing tool delay value for each shot. We fit the plot with a quadratic polynomial as in figure 3.4, which is then used to convert the x-pixel value of the cross-correlator beam to a timing delay. The data can then be binned according to timing delay.

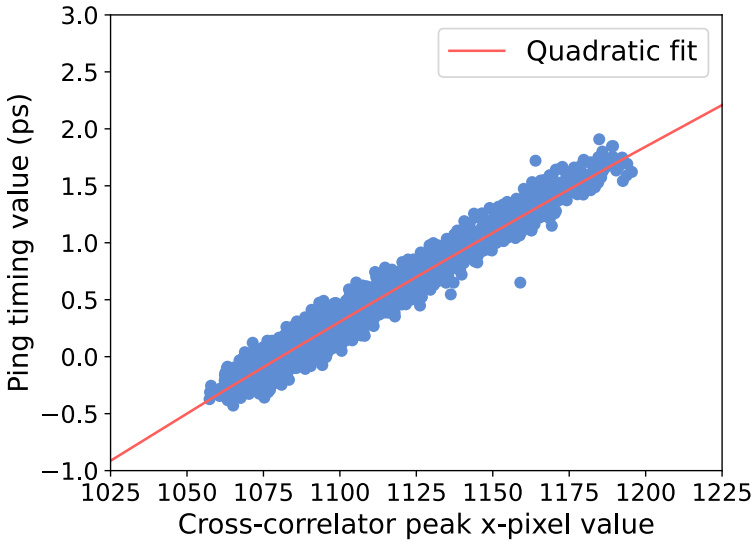

Figure 3.4: Cross-correlator timing calibration using the RF-timing tool delay value.

During our first experimental run, we delayed the laser pulse before it reached the cross-correlator based timing monitor. As a result, cross-correlator signal only existed for a small window during the scan as in figure 3.5. For these scans, we used the RF-timing tool to sort the data at the expense of accuracy, as there was too little data to meaningfully sort using the cross-correlator signal. Where the laser is delayed after the diagnostic beam is separated as in our 2nd and 3rd experimental

runs, the delay motor position Δd is summed with the cross-correlator timing delay as,

$$\Delta t_{\text{pump-probe}} = \Delta t_{\text{x-corr}} - \frac{2\Delta d}{c} \tag{3.1}$$

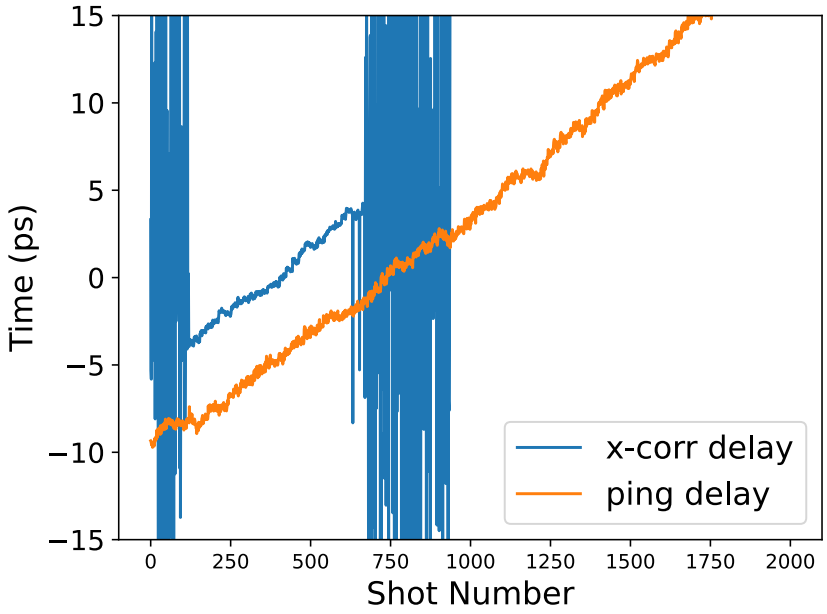

Figure 3.5: RF and cross-correlator timing values for each shot from a scan over pump-probe delays. The cross-correlator signal appears on the camera for a small window.

3.2 Diffraction Image Calibration

The raw data for each shot contains a 2D detector image showing the powder diffraction pattern. This data is some number of counts for each pixel on the detector. Although the detector is at some arbitrary position and angle with respect to the sample, we know that the diffraction rings are defined by scattering vectors with magnitude q making an angle 2θ with the probe beam. For the data to be physically meaningful, it should be interpreted based on the q-value at each point on the detector.

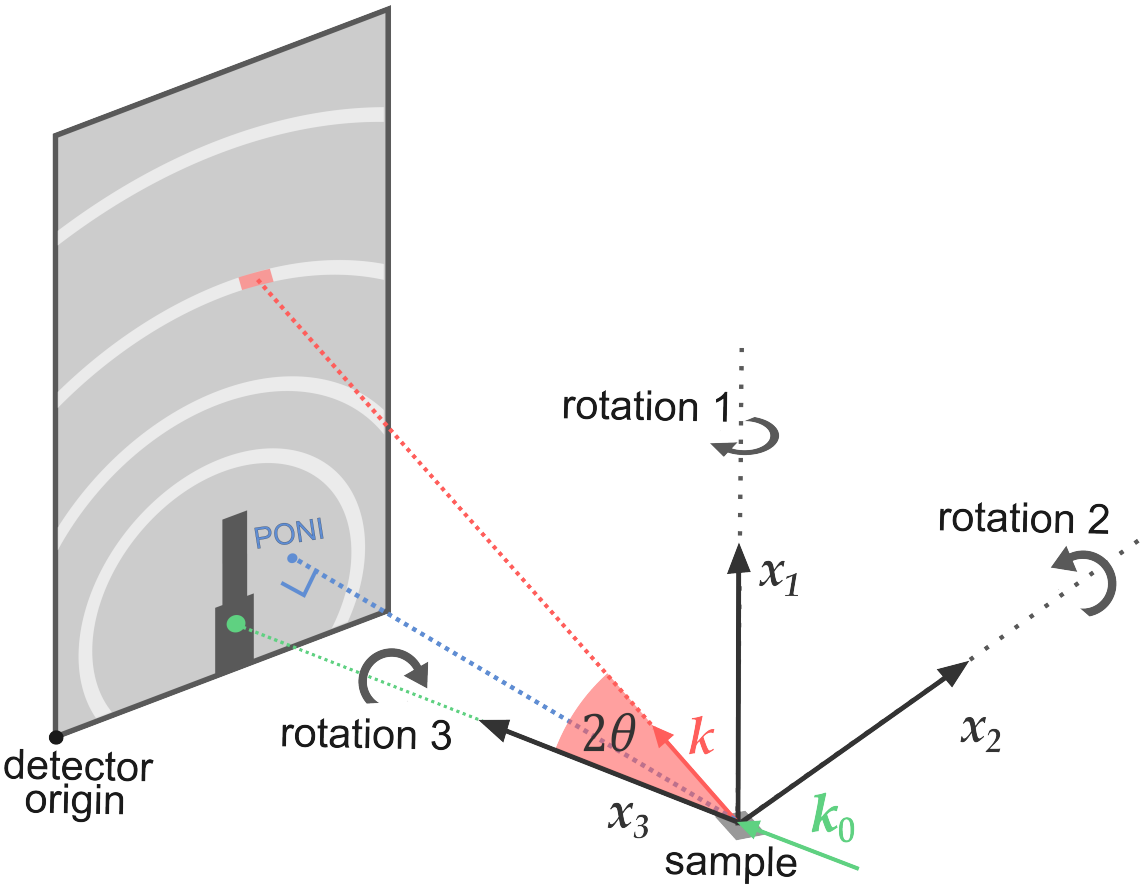

Figure 3.6: Diagram showing parameters needed to calibrate detector position to scattering vector amplitude. These parameters are the distance between the sample and the PONI (point of normal incidence), the coordinates of the PONI, and the three rotations as shown.

To perform this calibration, the pyFAI python library was used [39]. The pyFAI calibration tool computes the experimental geometry shown in figure 3.6 given the q values of the diffraction rings on a detector image. The unit cell length of the rock-salt GST is known to be $a = 6.01$ Å[40], using equation 1.30, the characteristic scattering vector magnitude q and lattice spacing d_{hkl} of each ring can be calculated.

We summed images from 2020 shots to create the summed detector image in figure 3.7. We then input the values from table 3.1 into a calibrant file, input the dimen-

Table 3.1: Planar spacing and scattering vector magnitude for the first six allowed diffraction rings for cubic rock-salt GST ($a = 6.01$ Å).

Reflection (hkl)	d_{hkl} (Å)	q (Å^{-1})
(111)	3.47	1.81
(200)	3.01	2.09
(220)	2.12	2.96
(311)	1.81	3.47
(222)	1.74	3.62
(400)	1.50	4.18

sions and pixel sizes of the Pilatus detector, then masked out the beamstop and unwanted reflection from silicon substrate. We input the X-ray photon energy (8 keV), and manually select points on the rings, the pyFAI software can then fit curves to the rings, and output the parameters shown in 3.6. These steps are illustrated in figure 3.8. These results are saved in a `.poni` file, which we use for performing azimuthal integration with pyFAI, determining the average intensity per pixel at each q value. The calibration output for one of our experiments is shown in appendix A.

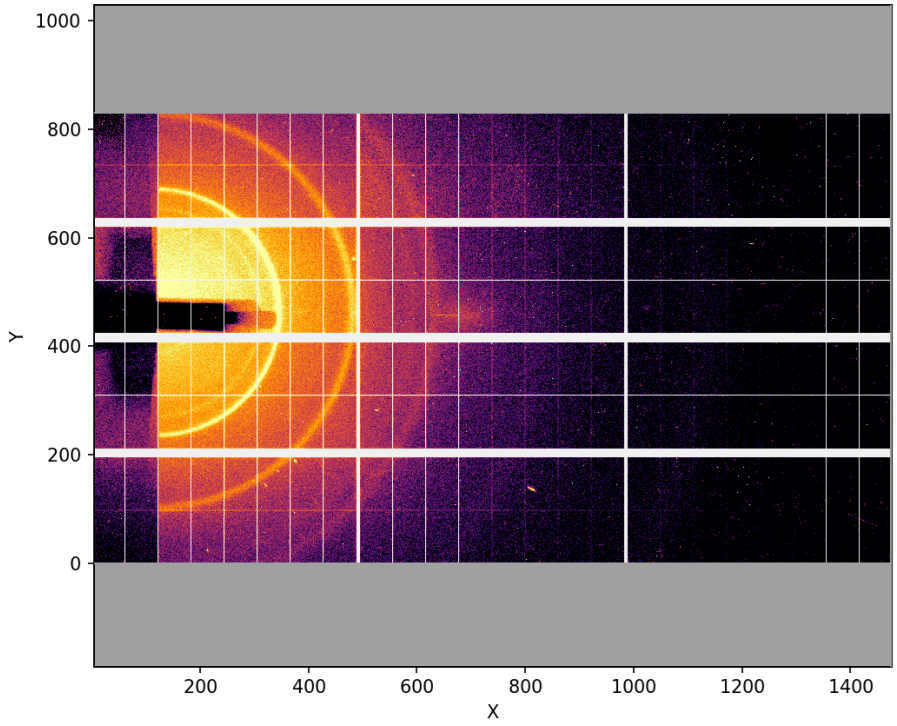

Figure 3.7: Summed detector image for use in pyFAI calibration showing clearly the first 4 allowed reflections from rock-salt GST.

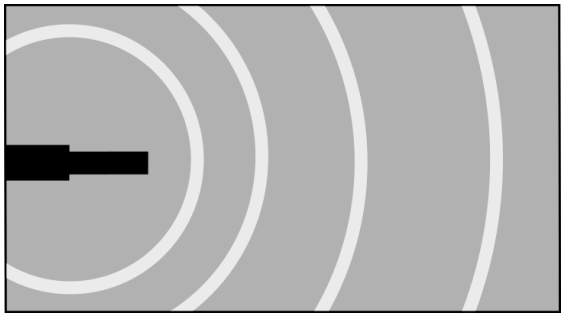

(a) Detector image

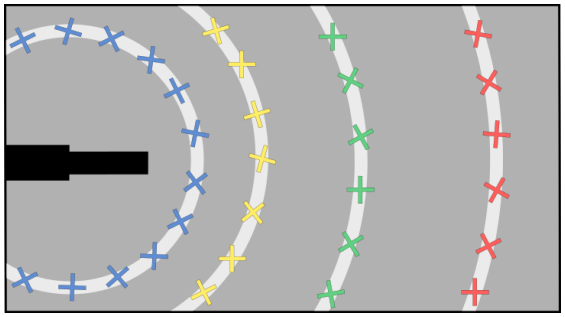

(b) Manually selecting points on the diffraction rings

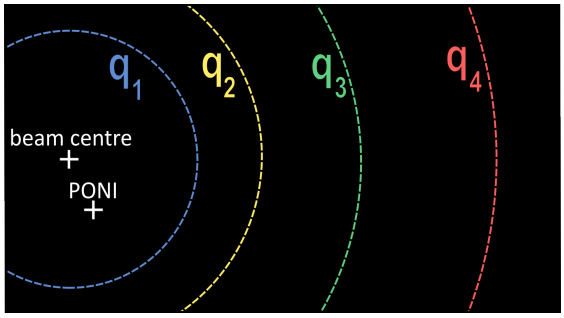

(c) pyFAI fits curves to the diffraction rings, and computes the experimental geometry

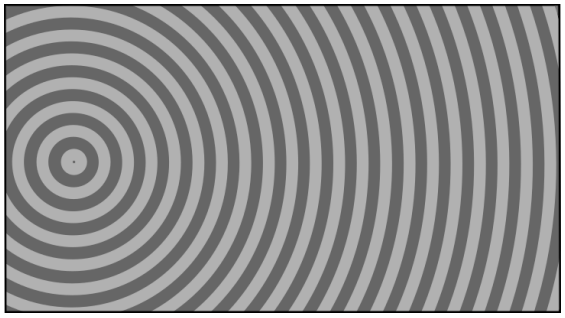

(d) q-bins on the detector surface

Figure 3.8: The pyFAI calibration tool is used to assign q-values to each point on the detector surface, and to compute the experimental geometry given the q-values and locations of the Bragg peaks.

3.3 Data Reduction and Azimuthal Integration

Given the detector image, and a pump-probe delay value for each shot, we assign each image to a timing bin, while also accumulating the number of shots per bin for later normalisation. The pyFAI `integrate1d_ng` function takes the sum of the images in each timing bin, and produces a one-dimensional diffraction profile by averaging detector pixels within radial bins of constant scattering vector.

It should be said explicitly that this intensity value is an average of the counts per pixel that have fallen into each radial (q) bin. We normalise the resulting I(q) by dividing by the number of shots assigned to each timing bin. The data can now be saved as a 2D q-t map, as visualised in figure 3.9.

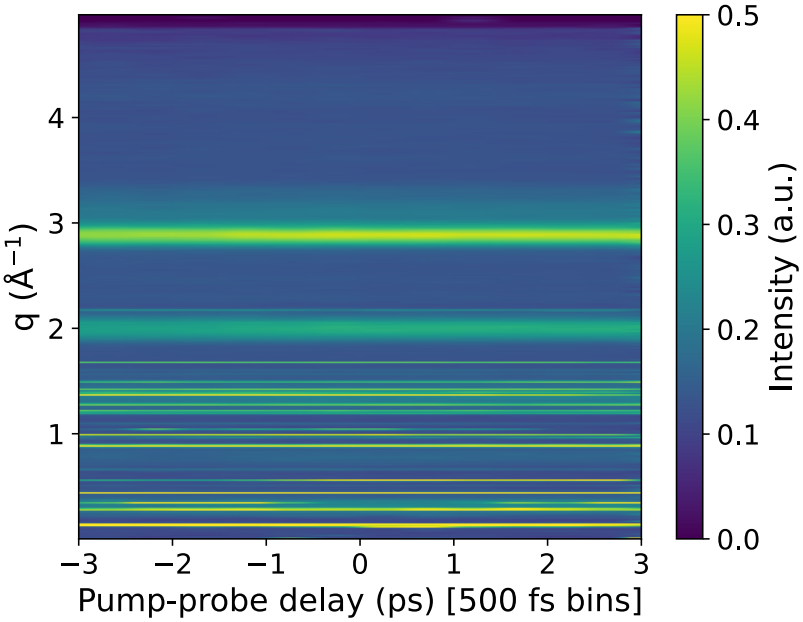

Figure 3.9: Two-dimensional q-t map representation of scan data from our second experimental run at laser fluence 50 mJ/cm^2. The region of interest in this work is from $q = 2.3$ Å^{-1} to $q = 2.8$ Å^{-1}.

Through this process, we condense gigabytes of data for each scan to kilobytes. By taking vertical slices of the q-t map, we generate 1D plots of intensity as a function of q for a some timing delay bin. One of these plots is shown in figure 3.10. Horizontal slices of the q-t map represent the intensity fluctuation for a given q value as a function of pump-probe delay.

By summing a band of q values over a region of interest, such as a Bragg peak, we can observe the time-dependent behaviour of this feature. This is shown in figure 3.11, where data from a band of q values in the above q-t map are summed to create a 1D plot. In practice, we sum data from many scans to improve signal-to-noise and

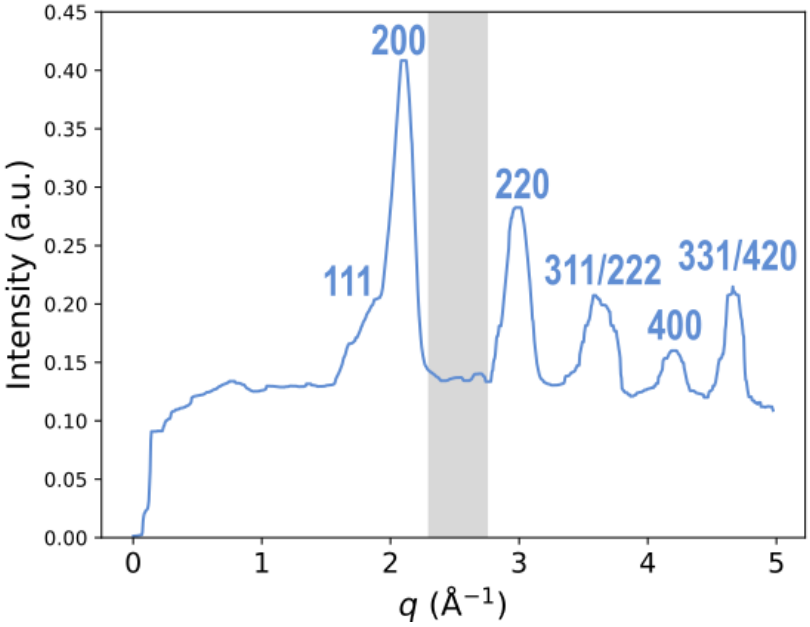

Figure 3.10: 1D plot of intensity as a function of scattering angle for rock-salt GST, a median filter was applied to remove noise. The Bragg peaks are labelled with *hkl* values. The diffuse scattering region highlighted in grey is the focus of this work.

time resolution.

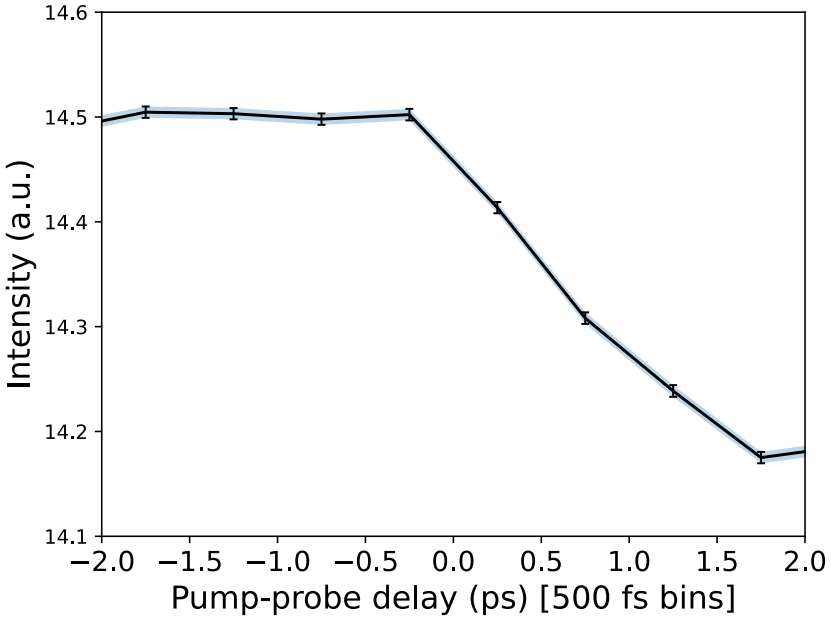

Figure 3.11: Time-dependent behaviour of the 200 peak intensity, 2.0 $Å^{-1} < q < 2.2$ $Å^{-1}$ in a group of scans from our second experimental run.

3.4 Error Analysis

As we are measuring a relatively weak diffuse scattering signal, we expect the dominant source of uncertainty to arise from shot-to-shot variations in the number of X-ray photons falling on each pixel. This includes photon shot noise, and genuine fluctuations in the sample response, such as those caused by damage. It also accounts for pulse-to-pulse X-ray/laser intensity fluctuations and detector noise, but these are expected to be relatively small in comparison.

When each shot is assigned to a pump-probe delay bin, the intensity and squared intensity of every detector pixel are accumulated over all images contributing to that bin. We then estimate the variance of each detector pixel using the unbiased sample variance. The pixel variance over N shots in a timing bin is

$$\sigma^2_{\text{pixel}} = \frac{\sum_{i=1}^{N} I_i^2 - \frac{1}{N}(\sum_{i=1}^{N} I_i)^2}{N-1} \tag{3.2}$$

The pixel variances were propagated through the same azimuthal integration procedure described above to obtain the variance within each radial bin $\sigma^2(q)$. Where we are interested in looking at the intensity over a region $q_{\text{min}} < q_i < q_{\text{max}}$, the uncertainty of the integrated intensity was calculated by adding the variances in quadrature,

$$\sigma_{\text{ROI}} = \sqrt{\sum_i \sigma^2_{\text{mean}}(q_i)} \tag{3.3}$$

These uncertainties are shown as the error bars on the time-dependent intensity plots shown in this work.

Chapter 4

Results

4.1 First Experimental Run

As previously discussed, the following plots show the intensities of the region between the 200 and 222 peaks on the 2D diffraction image. The scans in this run were post-sorted using the less accurate RF-timing tool. The speed of the intensity rise cannot therefore be well resolved, so the presence and magnitude of the rise are the points of discussion in this section.

Our first measurements were on stoichiometric GST, with varying laser fluence. Both of the plots in figures 4.1a and 4.1b show a 1-2% intensity rise in the region of interest. The 10 mJ cm^{-2} scans have too little data to meaningfully pinpoint time zero, but the 15 mJ cm^{-2} show a clear rise over $\sim$ 2 ps. This suggests that the diffuse signal appears for pump intensities as low as 10 mJ cm^{-2}. Further measurements

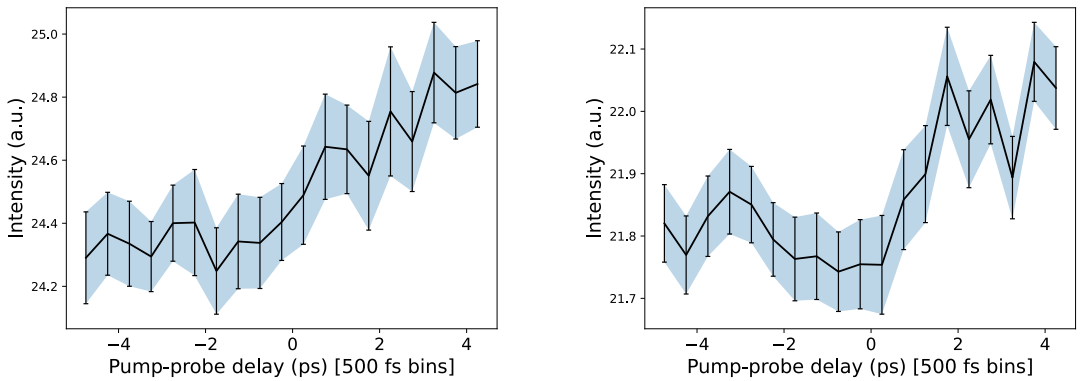

(a) 4 scans at 10 mJ cm^{-2}

(b) 23 scans at 15 mJ cm^{-2}

Figure 4.1: Diffuse scattering intensity from stoichiometric GST in for scattering vector 2.3 Å^{-1} $< q <$ 2.75 Å.

were done on a germanium-rich GST sample at varying laser fluence. The data shown in figure 4.2a does not show significant evidence of a rise in diffuse scattering for 5 mJ cm^{-2} laser fluence. At 10 mJ cm^{-2}, a small $\sim$0.6% rise can be seem. At 25 and 35 mJ cm^{-2}, there is a $\sim$2.6% intensity increase. These scans show that the rise

is more significant for higher pump fluences, and resolvable with data from fewer scans.

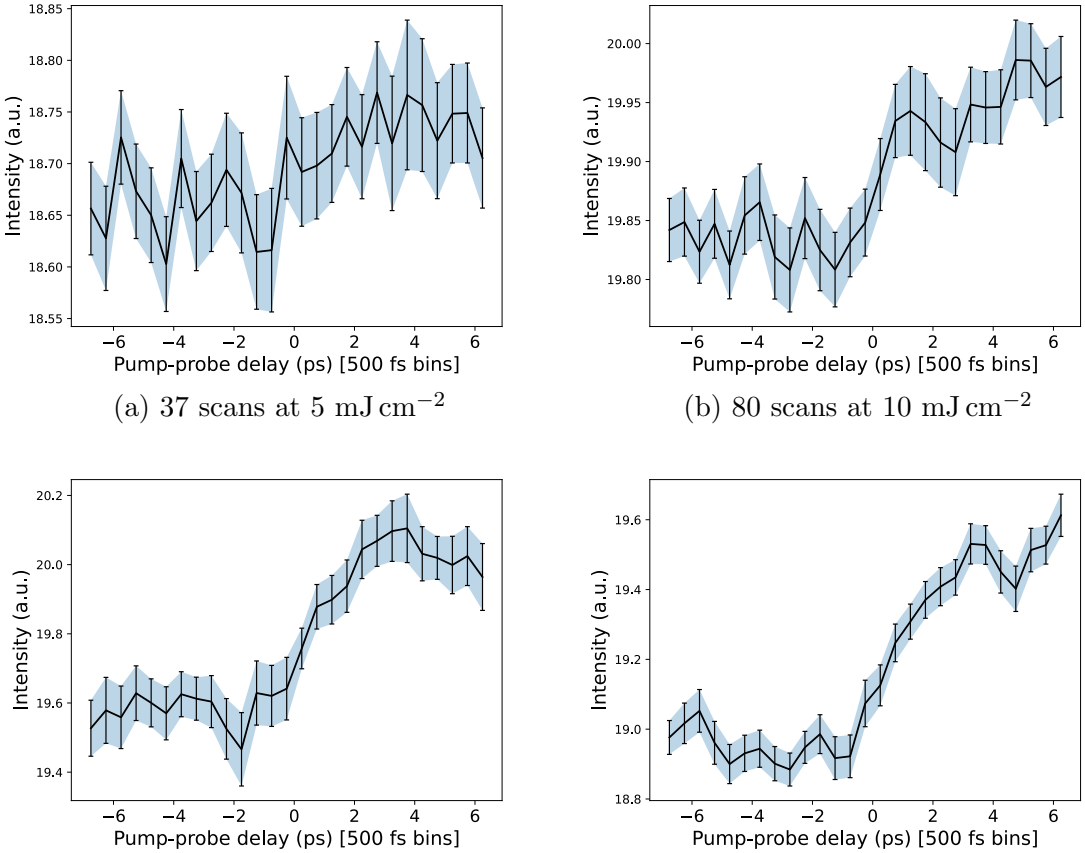

(a) 37 scans at 5 mJ cm^{-2}

(b) 80 scans at 10 mJ cm^{-2}

(c) 16 scans at 25 mJ cm^{-2}

(d) 28 scans at 35 mJ cm^{-2}

Figure 4.2: Time evolution of diffuse scattering intensity from germanium enriched GST for scattering vector 2.3 Å^{-1} $< q <$ 2.75 Å using 500 fs timing bins.

The data from 4.2c is presented in figure 4.3 as intensity in each radial bin for 3 different time slices. This shows that the rise in diffuse scattering occurs relatively uniformly in the region of interest.

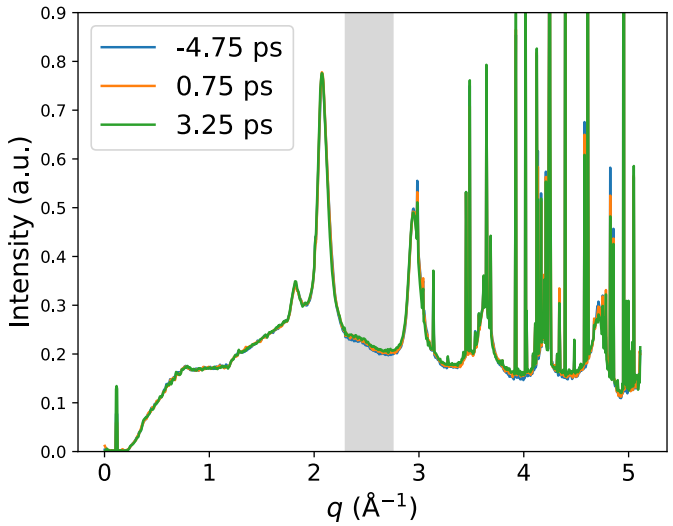

(a) Over the full detector.

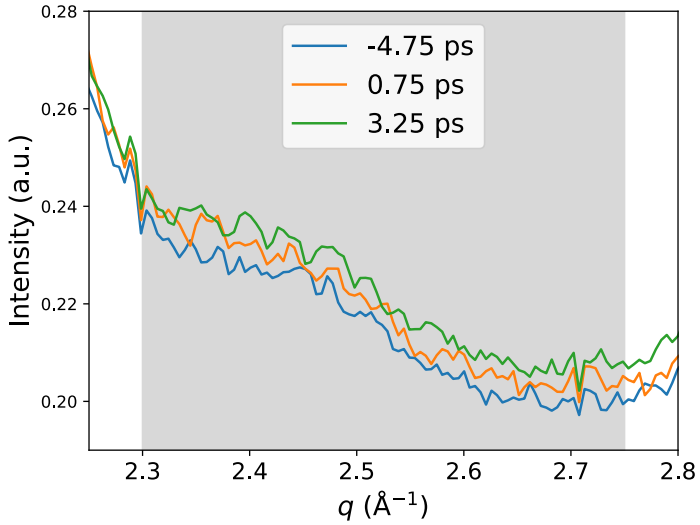

(b) Within the region of interest.

Figure 4.3: Radial intensity profiles, $I(q)$, before pumping, shortly after pumping, and approximately 3 ps after excitation with a 25 mJ cm^{-2} laser pulse.

4.2 Second Experimental Run

The data presented here was sorted using he cross-correlator based timing tool. The scans in figure 4.4 were taken at a 0.4° X-ray angle than the typical $\sim 1°$. The data from these scans is not sufficient to show a pump-induced intensity rise in the region of interest.

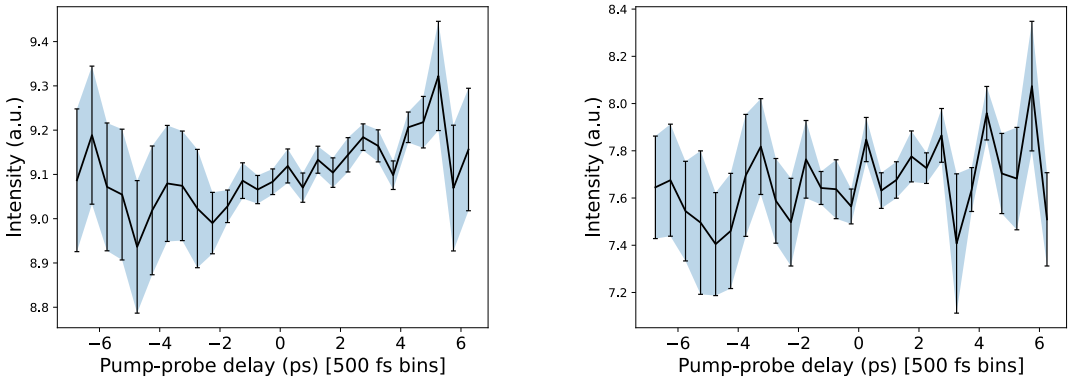

(a) 4 scans at 9 mJ cm^{-2} (b) 6 scans at 17 mJ cm^{-2}

Figure 4.4: Diffuse scattering behaviour at 0.4° of stoichiometric GST in 2.3 Å^{-1} $< q <$ 2.75 Å^{-1}.

We switched to a germanium-rich GST sample, and increased the laser fluence to 22.5 mJ cm^{-2}. Here, the signal-to-noise was sufficiently high that a $\sim$ 2% rise in diffuse scattering can be seen in some single scans, as in figure 4.5. The rise can now be seen to occur within 500 fs.

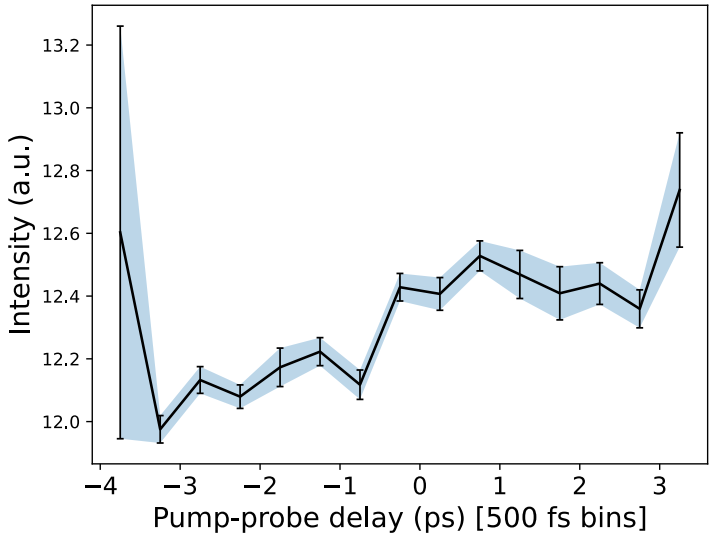

Figure 4.5: Diffuse scattering rise in single pump-probe delay scan in 2.3 Å^{-1} $< q <$ 2.75 Å^{-1} with laser fluence 22.5 mJ cm^{-2}.

This timing resolution can be improved by summing data from repeated scans with these same conditions. To this end, 108 further scans were made. In figure 4.6, the behaviour of the diffuse scattering rise can be resolved. An initial $\sim 1\%$ intensity rise is followed by a slower $\sim 2\%$ intensity rise. The initial fast rise is of particular

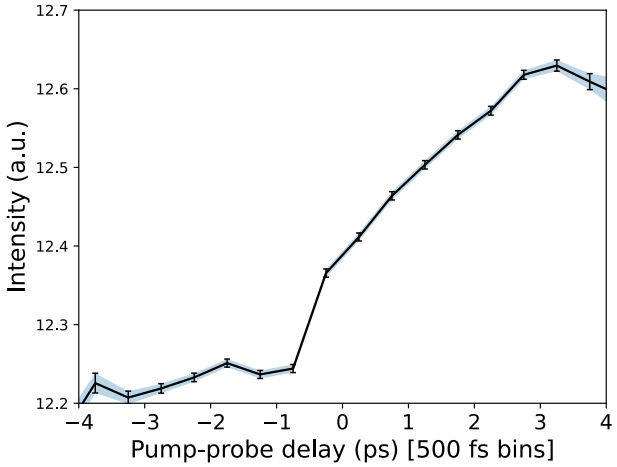

Figure 4.6: Diffuse scattering rise in 109 pump-probe delay scans in scattering vector range 2.3 $\text{Å}^{-1} < q < 2.75$ Å^{-1} with laser fluence 22.5 $\text{mJ}\,\text{cm}^{-2}$ and X-ray incidence angle $\sim 1°$.

interest, as this defines the time-zero window that we can define by using GST as a time-zero monitor. Figure 4.7 shows the fast rise region with 30 fs timing bins, the uncertainty limit of the cross-correlator timing tool. This aligns with the result from Kroon et. al. [33], a rise in diffuse scattering in this region occurs in <70 fs.

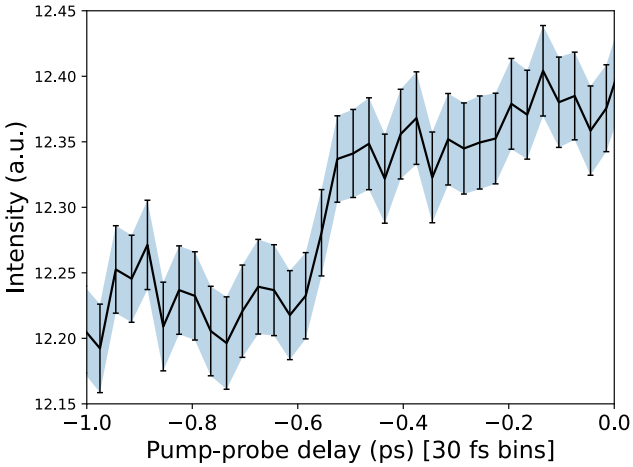

Figure 4.7: Fast 1% rise in diffuse scattering intensity in range 2.3 $\text{Å}^{-1} < q < 2.75$ Å^{-1} driven by laser fluence 22.5 $\text{mJ}\,\text{cm}^{-2}$.

As previously discussed, an increase in diffuse scattering intensity will coincide with a reduction in Bragg peak intensity. The intensity of the 220 peak in this same data is shown in figure 4.8. This intensity drop is slower than the rise seen in ROI.

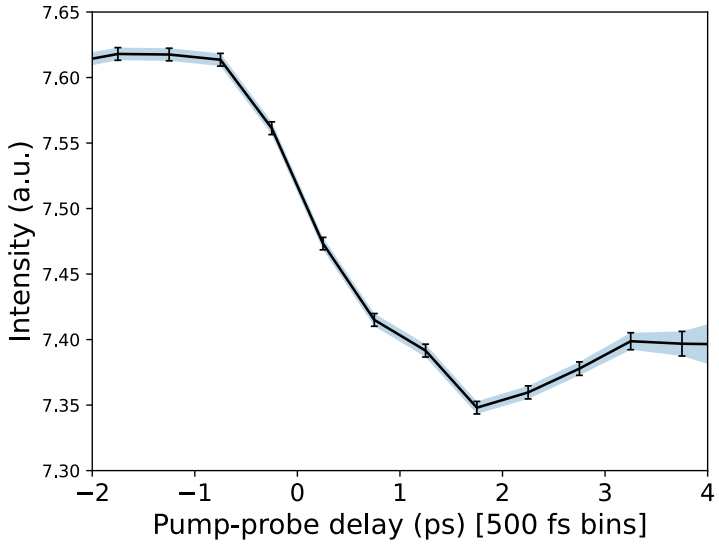

Figure 4.8: 220 peak intensity, 2.85 $\text{Å}^{-1} < q < 3.00\ \text{Å}^{-1}$.

Another view of this behaviour is shown in figure 4.9. Once again, a relatively uniform increase is evident across the q values in the ROI. In contrast, comparing the Bragg peaks before and after time zero, there is no dimming until ∼500 fs after the pump and probe beams are coincident on the sample. This is shown using the same timing bins in figure 4.10

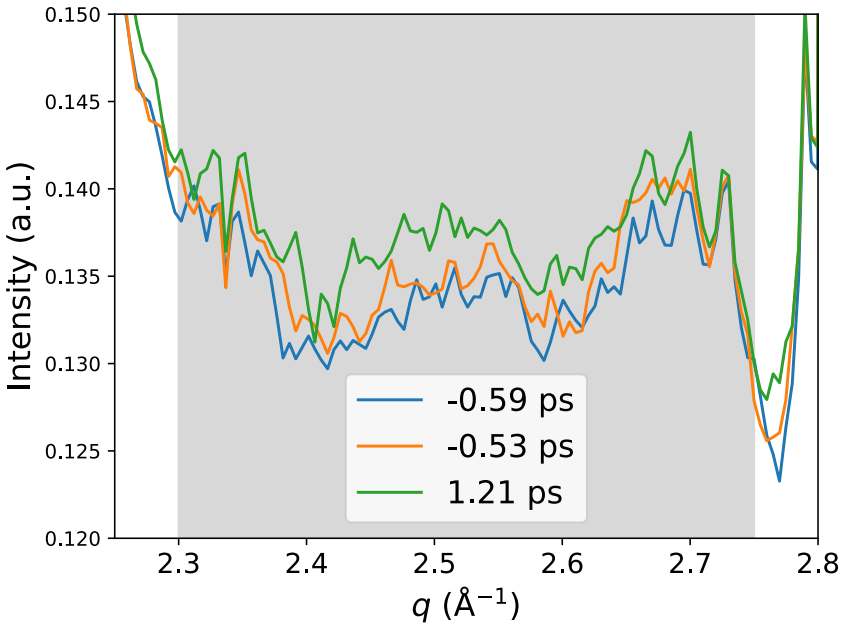

Figure 4.9: Three snapshots of the diffuse scattering region between the 200 and 220 peaks. The initial fast rise, and continued slower rise, are evident across the region.

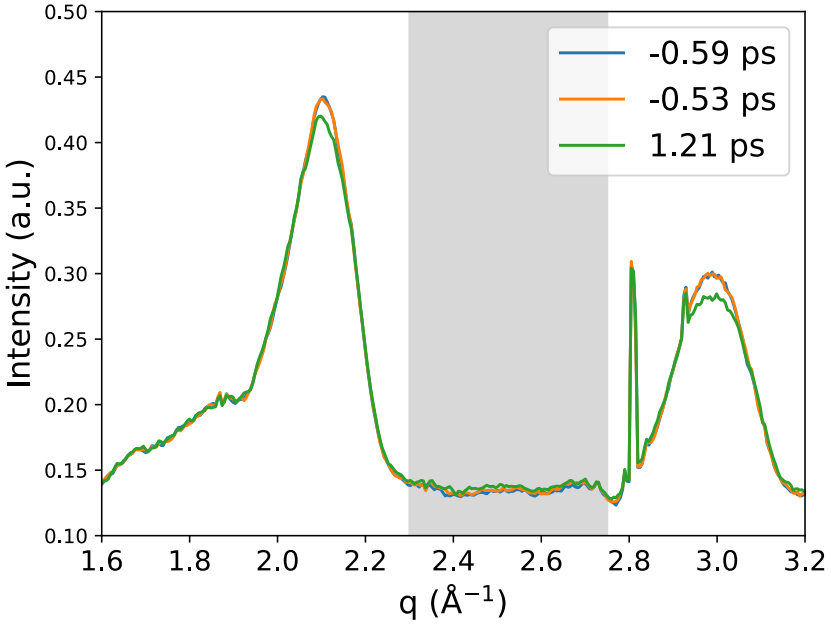

Figure 4.10: The 200 and 220 peaks in three snapshots. The first are before, and after time-zero, and the final is ∼700 fs later.

4.3 Third Experimental Run

The primary purpose of our third experimental run was to observe lattice distortions in stoichiometric GST after pumping with a 1500 nm OPA beam. However, some of the results are still of interest to this work. These measurements were taken in vacuum, so we can observe the diffuse rise with a lower noise floor. We now observe

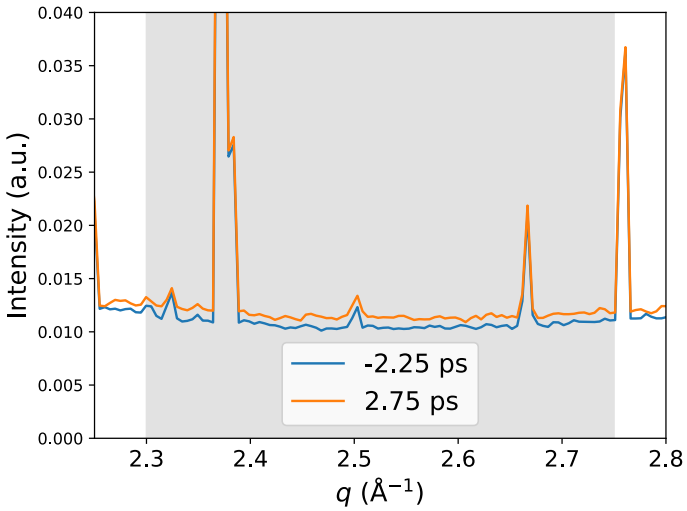

Figure 4.11: Diffuse scattering in GST before and after pumping with a 1500 nm laser in vacuum.

several distinct peaks in the diffuse region, which seem to undergo the same intensity increase as the surrounding region under pumping. The largest peak is close to the 101 peak of hexagonal GST, at = 2.33Å^{-1}. It could be the case that the sample underwent partial crystallisation due to cycles of pumping/heating/cooling, causing a small amount of hexagonal GST to form.

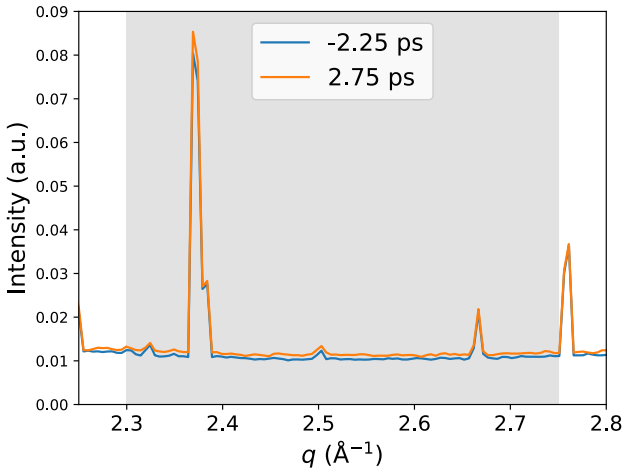

Figure 4.12: Previously unseen peaks in diffuse scattering region of interest.

During this run, the scans were completed over a number of fluence values. Here, we sum together those scans which used a pump fluence $< 10\ \mathrm{mJ\,cm^{-2}}$, and those using pump fluence $> 10\ \mathrm{mJ\,cm^{-2}}$. The familiar rise behaviour is reproduced by the higher fluence scans in figure 4.13.

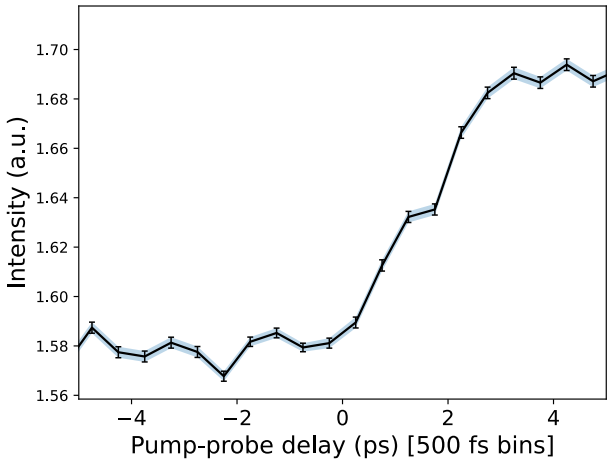

Figure 4.13: Diffuse scattering rise between 200 and 220 peaks of stoichiometric GST from 92 delay scans at fluences between 11 $\mathrm{mJ\,cm^{-2}}$ and 30 $\mathrm{mJ\,cm^{-2}}$ pump laser fluence.

The data in figure 4.14 shows fluctuations that are not accounted for by shot-to-shot variance. Since these 26 scans were taken separately over the course of days, any drift in the cross-correlator signal may be too significant to meaningfully sum the data.

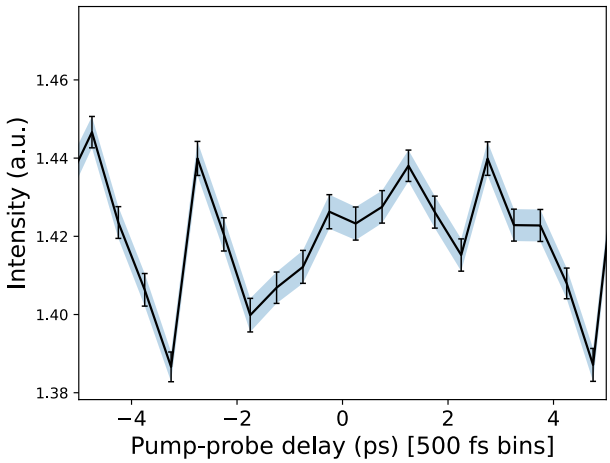

Figure 4.14: Diffuse scattering signal between 200 and 220 peaks of stoichiometric GST from 11 delay scans at 3 $\mathrm{mJ\,cm^{-2}}$ pump laser fluence, and 21 delay scans at 6 $\mathrm{mJ\,cm^{-2}}$ fluence.

We used a heater to change the temperature of the sample. Figure 4.15 shows that the same rise behaviour can be observed at 100°C.

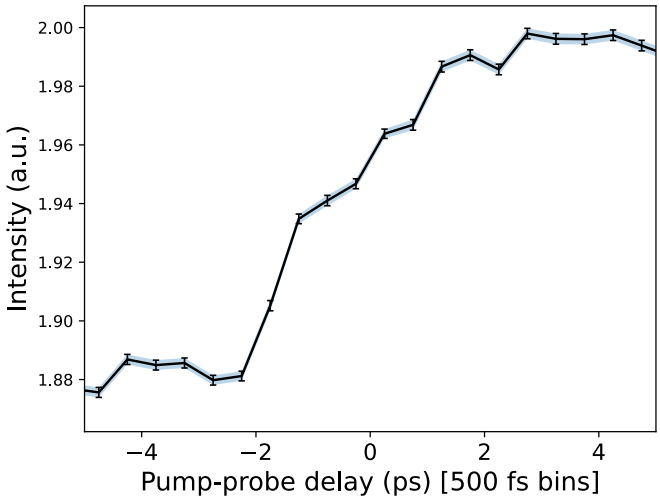

Figure 4.15: Intensity between 200 and 220 peaks from 175 delay scans at 100°C using a range of laser fluences from 3 to 30 $\mathrm{mJ\,cm^{-2}}$.

In these scans, we are able to resolve an intensity rise between the peaks at low pump fluence, albeit with low temporal resolution. This suggests that the fast rise may be easier to induce at high temperatures.

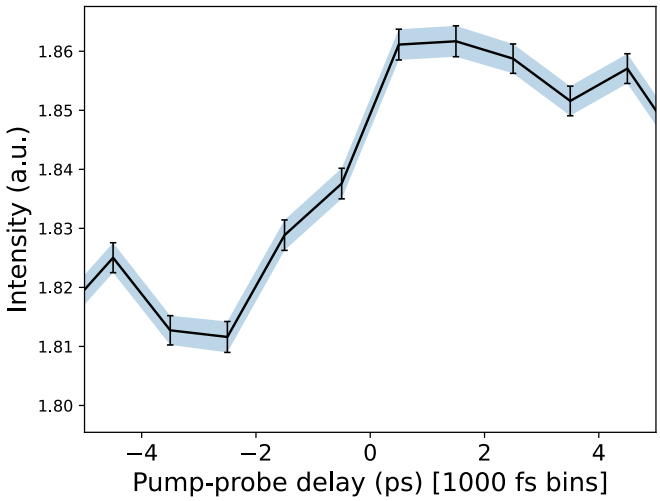

Figure 4.16: Intensity between 200 and 220 peaks from 30 delay scans at 100°C using pump laser fluences from 3 to 6 $\mathrm{mJ\,cm^{-2}}$.

Chapter 5

Discussion & Conclusions

5.1 Experimental Conditions for Time-Zero Monitoring

Pump laser fluence was found to have a strong influence on the detectability of the diffuse scattering rise. However, we did not note a significant improvement in signal-to-noise for fluences above 22.5 $\mathrm{mJ\,cm^{-2}}$. Since higher pump fluences contribute more to sample degradation, laser fluences close to this value are ideal for time-zero determination using GST.

Both stoichiometric and germanium-enriched GST produced a measurable diffuse scattering response. The two samples did not perform identically, but were also not measured in identical conditions. There is no evidence to suggest that either sample performs better as a time-zero monitor.

The diffuse scattering rise could be observed at elevated sample temperature. This suggests that the rise can be measured under a wide range of experimental conditions.

5.2 Conclusions

The primary aim of this work was to investigate whether the transient diffuse scattering response of $Ge_2Sb_2Te_5$ (GST) could be used as a reliable timing tool for ultrafast pump-probe X-ray diffraction experiments at FemtoMAX. The time evolution of the diffuse scattering following femtosecond laser excitation under a range of experimental conditions was analysed. This work demonstrates that the diffuse scattering response can provide a fast, and reproducible signature of time zero.

A complete analysis pipeline was developed to process pump-probe diffraction data. This included shot-by-shot timing correction using the FemtoMAX cross-correlator, sorting detector images into pump-probe delay bins, azimuthal integration using `pyFAI`, and propagation of experimental uncertainties from detector images to the final time-dependent intensity plots. The resulting workflow provides an efficient

and reproducible method for analysing ultrafast diffraction data and can readily be applied at FemtoMAX.

Measurements performed during three beamtimes reproduced the characteristic ultrafast increase in diffuse scattering intensity that was previously reported for GST. A combination of data from more than one hundred delay scans allowed the initial diffuse scattering rise to be resolved using 30 fs timing bins. The rise was found to occur within >70 fs, in agreement with previous measurements at FemtoMAX. The corresponding decrease in Bragg peak intensity was seen to occur on a much slower timescale. This demonstrates that the diffuse scattering response is fast enough to define the time-zero window for ultrafast X-ray diffraction experiments.

Several limitations were identified during this work. While shot-to-shot statistical uncertainties were propagated throughout the analysis, some measurements exhibited fluctuations larger than those expected from these alone. This is likely to arise from changes in experimental conditions, such as drift in the timing diagnostics or variations in sample quality.

Overall, this work demonstrates that diffuse scattering in GST is a practical and reliable timing monitor for femtosecond pump-probe X-ray diffraction at FemtoMAX.

5.3 Outlook

The results presented in this work establish transient diffuse scattering from GST as a promising time-zero monitor, but several questions remain concerning the physical origin and practical optimisation of the technique. The most immediate area for future work is to determine the structural dynamics behind the fast change of the diffuse signal.

A more direct comparison between stochiometric and germanium-enriched GST in identical conditions could determine whether one composition is a more suitable time-zero monitor.

Future studies would benefit from improved monitoring of long-term timing stability. Repeated measurements of GST throughout a beamtime could be used to quantify cross-correlator drift, and hence determine an appropriate recalibration interval.

Appendix A

PyFAI Output

This is the output of the pyFAI calibration software for one of our experiments. We export this information in a `.poni` file, and use it to integrate the detector image over each scattering vector q bin.

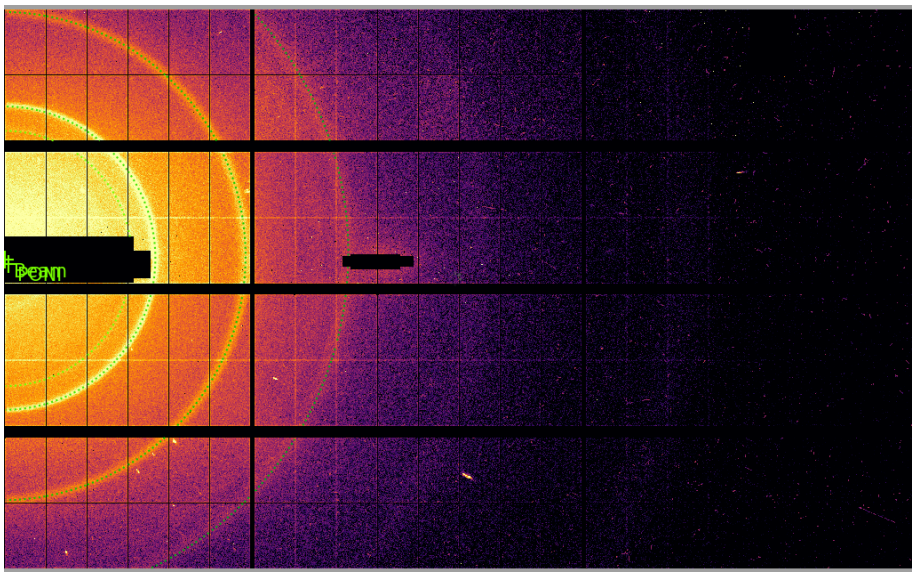

Figure A.1: Output from pyFAI calibration tool, showing fit curves, beam centre, and PONI.

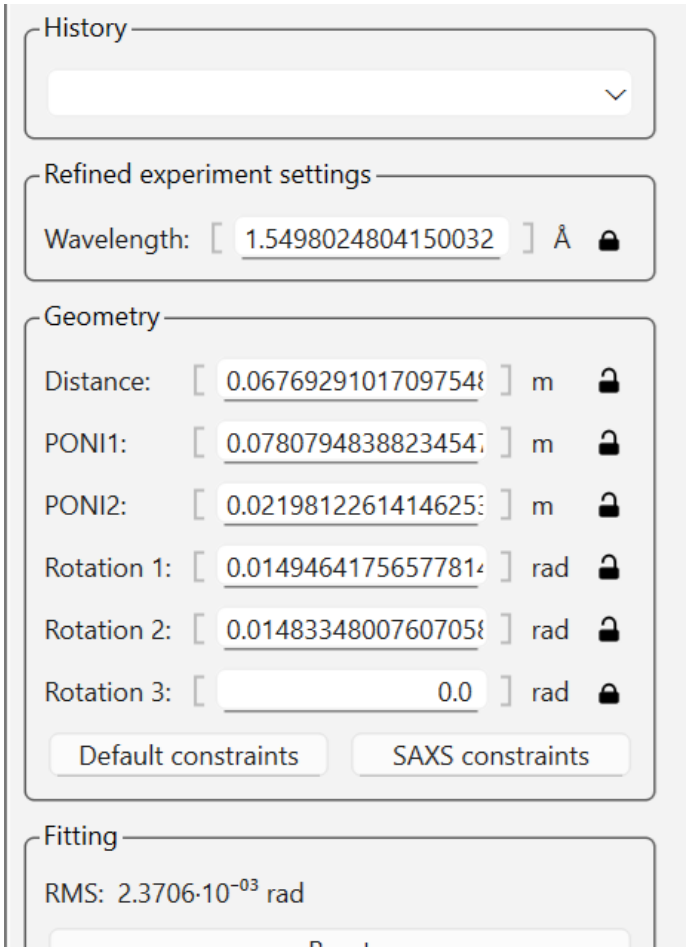

Figure A.2: Output from pyFAI calibration tool showing experimental geometry.

Appendix B

Analysis Code

The Python notebook implementing the analysis pipeline used in this work can be found at `https://github.com/sallydolanphysics/Lund-University`.

Appendix C

Plagiarism Declaration

I confirm that the work presented in this thesis is my own and that it has not been plagiarised.

References

Books

[1]B. E. Warren, *X-ray diffraction* (Dover, New York, 1990).

[2]C. Kittel, *Introduction to solid state physics* (Wiley, Hoboken, Nj, 2005).

Articles, proceedings and theses

[1]A. M. Lindenberg, S. L. Johnson, and D. A. Reis, "Visualization of Atomic-Scale Motions in Materials via Femtosecond X-ray Scattering Techniques", Annual Review of Materials Research **47**, 425–449 (2017).

[2]E. Matsubara et al., "Initial Atomic Motion Immediately Following Femtosecond-Laser Excitation in Phase-Change Materials", Physical Review Letters **117**, 10.1103/physrevlett.117.135501 (2016).

[3]K. V. Mitrofanov et al., "Sub-nanometre resolution of atomic motion during electronic excitation in phase-change materials", Scientific Reports **6**, 10.1038/srep20633 (2016).

[4]C. Yang et al., "Melting domain size and recrystallization dynamics of ice revealed by time-resolved x-ray scattering", Nature Communications **14**, 10.1038/s41467-023-38551-0 (2023).

[5]T. A. Assefa et al., "Ultrafast x-ray diffraction study of melt-front dynamics in polycrystalline thin films", Science Advances **6**, 10.1126/sciadv.aax2445 (2020).

[6]F. Vidal et al., "Ultrafast Structural Dynamics along the - Phase Transition Path in MnAs", Physical Review Letters **122**, 10.1103/physrevlett.122.145702 (2019).

[7]M.-C. Lee et al., "Direct Observation of Coherent Longitudinal and Shear Acoustic Phonons in TaAs Using Ultrafast [x]-ray Diffraction", Physical Review Letters **128**, 10.1103/physrevlett.128.155301 (2022).

[8]T. Henighan et al., "Generation mechanism of terahertz coherent acoustic phonons in Fe", Phys. Rev. B **93**, 220301(R) (2016).

[9]R. Shayduk et al., "Femtosecond x-ray diffraction study of multi-THz coherent phonons in Sr[t]iO3", Applied Physics Letters **120** (2022).

[10]M. Kubli et al., "Kinetics of a Phonon-Mediated Laser-Driven Structural Phase Transition in Sn2P2Se6", Applied Sciences **9**, 525 (2019).

[11]Y. Kubota et al., "Suppression of atomic displacive excitation in photo-induced A1g phonon mode of bismuth unveiled by low-temperature time-resolved x-ray diffraction", Applied Physics Letters **122**, 10.1063/5.0136787 (2023).

[12]Y. Lee et al., "A comparative review of time-resolved x-ray and electron scattering to probe structural dynamics", Structural Dynamics **11**, 10.1063/4.0000249 (2024).

[13]A. A. Zholents and M. S. Zolotorev, "Femtosecond X-Ray Pulses of Synchrotron Radiation", Physical Review Letters **76**, 912–915 (1996).

[14]R. W. Schoenlein et al., "Generation of Femtosecond Pulses of Synchrotron Radiation", Science **287**, 2237–2240 (2000).

[15]K. Sokolowski-Tinten et al., "Femtosecond X-ray measurement of coherent lattice vibrations near the Lindemann stability limit", Nature **422**, 287–289 (2003).

[16]P. Emma et al., "First lasing and operation of an ångstrom-wavelength free-electron laser", Nature Photonics **4**, 641–647 (2010).

[17]T. Ishikawa et al., "A compact X-ray free-electron laser emitting in the sub-ångström region", Nature Photonics **6**, 540–544 (2012).

[18]H.-S. Kang et al., "Hard X-ray free-electron laser with femtosecond-scale timing jitter", Nature Photonics **11**, 708–713 (2017).

[19]W. Decking et al., "A MHz-repetition-rate hard X-ray free-electron laser driven by a superconducting linear accelerator", Nature Photonics **14**, 391–397 (2020).

[20]E. Prat et al., "A compact and cost-effective hard X-ray free-electron laser driven by a high-brightness and low-energy electron beam", Nature Photonics **14**, 748–754 (2020).

[21]C. Gahl et al., "A femtosecond X-ray/optical cross-correlator", Nature Photonics **2**, 165–169 (2008).

[22]T. Maltezopoulos et al., "Single-shot timing measurement of extreme-ultraviolet free-electron laser pulses", New Journal of Physics **10**, 033026 (2008).

[23]M. R. Bionta et al., "Spectral encoding of x-ray/optical relative delay", Optics Express **19**, 21855 (2011).

[24]M. Beye et al., "X-ray pulse preserving single-shot optical cross-correlation method for improved experimental temporal resolution", Applied Physics Letters **100**, 10.1063/1.3695164 (2012).

[25]O. Krupin et al., "Temporal cross-correlation of x-ray free electron and optical lasers using soft x-ray pulse induced transient reflectivity", Optics Express **20**, 11396 (2012).

[26]M. Harmand et al., "Achieving few-femtosecond time-sorting at hard X-ray free-electron lasers", Nature Photonics **7**, 215–218 (2013).

[27]J. C. P. Koliyadu et al., "Pump–probe capabilities at the SPB/SFX instrument of the European XFEL", Journal of Synchrotron Radiation **29**, 1273–1283 (2022b).

[28]P. F. Tavares et al., "The MAXIV storage ring project", Journal of Synchrotron Radiation **21**, 862–877 (2014).

[29]H. Enquist et al., "FemtoMAX – an X-ray beamline for structural dynamics at the short-pulse facility of MAX IV", Journal of Synchrotron Radiation **25**, 570–579 (2018).

[30]D. M. Fritz et al., "Ultrafast Bond Softening in Bismuth: Mapping a Solid's Interatomic Potential with X-rays", Science **315**, 633–636 (2007).

[31]S. W. Epp et al., "Time zero determination for FEL pump-probe studies based on ultrafast melting of bismuth", Structural Dynamics **4**, https://doi.org/10.1063/1.4999701 (2017).

[32]Å. U. J. Bengtsson et al., "Repetitive non-thermal melting as a timing monitor for femtosecond pump/probe X-ray experiments", Structural Dynamics **7**, https://doi.org/10.1063/4.0000020 (2020).

[33]D. Kroon et al., "A cross-correlator-based timing tool for FemtoMAX", Journal of Synchrotron Radiation **32**, 1052–1058 (2025).

[34]P. Ehrhart, "The configuration of atomic defects as determined from scattering studies", Journal of Nuclear Materials **69–70**, 200–214 (1978).

[35]F. Zamponi et al., "Femtosecond powder diffraction with a laser-driven hard X-ray source", Opt. Express **18**, 947–961 (2010).

[36]FemtoMAX beamline team, *FemtoMAX MAX IV beamline review report*, June 2024.

[37]M. Folk et al., "An overview of the HDF5 technology suite and its applications", Proceedings of the EDBT/ICDT 2011 Workshop on Array Databases, 36–47 (2011).

[38]S. van der Walt et al., "Scikit-image: image processing in Python", PeerJ **2**, e453 (2014).

[39]G. Ashiotis et al., "The fast azimuthal integration Python library:pyFAI", Journal of Applied Crystallography **48**, 510–519 (2015).

[40]V. Bragaglia et al., "Metal - Insulator Transition Driven by Vacancy Ordering in GeSbTe Phase Change Materials", Scientific Reports **6**, 10.1038/srep23843 (2016).